CONSTRUCTION OF A SCANNING TUNNELING MICROSCOPE AND FIRST RESULTS

A THESIS

SUBMITTED TO THE DEPARTMENT OF PHYSICS

AND THE INSTITUTE OF ENGINEERING AND SCIENCES

OF BILKENT UNIVERSITY

IN PARTIAL FULFILLMENT OF THE REQUIREMENTS

FOR THE DEGREE OF

MASTER OF SCIENCE

BY

Ahmet ORAL

January 1990

QC
173.4
.S94
O63
1990

CONSTRUCTION OF A SCANNING TUNNELING MICROSCOPE AND FIRST RESULTS

A THESIS

SUBMITTED TO THE DEPARTMENT OF PHYSICS

AND THE INSTITUTE OF ENGINEERING AND SCIENCES

OF BILKENT UNIVERSITY

IN PARTIAL FULFILLMENT OF THE REQUIREMENTS

FOR THE DEGREE OF

MASTER OF SCIENCE

By

Ahmet Oral

January 1990

GC
173.4
.S94
063
1990/C.1
B. SC58

to Berna...

I certify that I have read this thesis and that in my opinion it is fully adequate, in scope and in quality, as a thesis for the degree of Master of Science.

Assoc. Prof. Dr. Recai M. Ellialtıoğlu
(Principal Advisor)

I certify that I have read this thesis and that in my opinion it is fully adequate, in scope and in quality, as a thesis for the degree of Master of Science.

Prof. Dr. Cemal Yalabık

I certify that I have read this thesis and that in my opinion it is fully adequate, in scope and in quality, as a thesis for the degree of Master of Science.

Prof. Dr. Abdullah Atalar

Approved for the Institute of Engineering and Sciences:

Prof. Dr. Mehmet Baray
Director of Institute of Engineering and Sciences

ABSTRACT

CONSTRUCTION OF A SCANNING TUNNELING MICROSCOPE AND FIRST RESULTS

Ahmet Oral
M. S. in Physics
Supervisor: Assoc. Prof. Dr. Recai M. Ellialtıoğlu
January 1990

In this thesis, construction of a Scanning Tunneling Microscope in air is explained. A step motor sample approach mechanism and a tripod scanner are used in the construction.

Atomic resolution images of graphite samples are obtained in both constant current and constant height modes. Loss of trigonal symmetry in some Graphite images are also observed. This anomaly is attributed to the multiple atom tip or slipped top layer of Graphite.

Keywords: Scanning Tunneling Microscope, Tunneling, Piezo, Scanner, Graphite, Tip.

ÖZET

BİR TARAMALI TÜNELLEME MİKROSKOBU YAPIMI VE İLK SONUÇLARI.

Ahmet Oral
Fizik Yüksek Lisans
Tez Yöneticisi: Doç. Dr. Recai M. Ellialtıoğlu
Ocak 1990

Bu tezde, atmosferde çalışan bir Taramalı Tünel Mikroskobu yapımı açıklanmıştır. Tasarımda adım motorlu bir örnek yaklaştırma sistemi ile piezoelektrik tüplerden yapılmış bir üçayak tarama sistemi kullanılmıştır.

Grafit yüzeyinin atomsal çözünürlükteki görüntüleri değişmez akım ve değişmez yükseklik yöntemleriyle elde edilmiştir. Bazı Grafit yüzeylerinde üçgensel simetrinin kaybolduğu gözlenmiştir. Bu olağandışılık çok atomlu uca yada kaymış üst tabakaya bağlanmıştır.

Anahtar sözcükler: Taramalı Tünel Mikroskobu, Tünelleme, Piezo, Tarama sistemi, Grafit, Uç.

ACKNOWLEDGEMENT

I am grateful to Assoc. Prof. Dr. Recai M. Ellialtıoğlu for the invaluable guidance, encouragement, and above all, for the enthusiasm which he inspired on me during the study.

I would like to express my deeep gratitude to İsmet Kaya for his collaboration, motivation and his friendly personality.

I would like thank İsmail Doğru, METU Physics Department, for his advices and machining the STM.

I debt special thanks to Prof. Dr. Salim Çıracı, Prof. Dr. Cemal Yalabık and Inst. Erkan Tekman for their encouragement and remarks.

Last but not the least, I wish to thank to Berna Ciner for her helps and continuous moral support.

Contents

List of Figures

Chapter 1

Introduction

The transmission of particles across a classically forbidden region in which the particle can not exist, is called tunneling. The phenomena is purely Quantum Mechanical and is a direct consequence of the wave–particle duality.

Tunneling phenomena has been proposed by Oppenheimer [1] in 1928 to explain autoionization of Hydrogen atoms in very high electric fields. Fowler and Nordheim [2] have explained electron emission from metals under intense electric fields with tunneling to the vacuum, which was observed in 1922.

The first experimental observation of tunneling in solids has been achieved by Esaki [3] in 1958. His tunnel diode is one of the most important application of tunneling, which led today novel tunneling devices. In 1960, Giaver [4] has observed superconducting energy gap by using a superconductor–insulator–normal metal junction (SIN) and developed tunneling spectroscopy. In 1962, Josephson [5] has investigated novel features in SIS structures, later called Josephson junctions. Esaki, Giaver and Josephson were awarded with Nobel Prize in Physics in 1973 for their fundamental works on tunneling.

Devices, using tunneling phenomena, such as MIM diodes, hot electron transistors, SQUID's were also developed in 70's. Another application of the tunneling is Inelastic Electron Tunneling Spectroscopy (IETS) [6]. Organic molecules are adsorbed on an oxide surface of a MIM junction, before the last

electrode was formed. If energy of the tunneling electrons coincides with one of the vibrational energy levels of the adsorbate, tunneling electrons interact with the molecule and tunneling current changes. Changes in the tunneling current can be observed if d^2I/dV^2 is plotted as a function of voltage. Therefore, vibrational energy levels of the adsorbate can be obtained.

Tunneling experiments are performed with oxide barriers until 80's. The vacuum, instead of an oxide as a barrier, is very attractive for many reasons. First of all, the barrier width can be changed easily. Bare surface properties are not affected by the oxide layers. However, vacuum tunneling was not achieved due to technical problems, mainly vibration isolation until early 80's.

Young *et al.* [7] developed a microscope, called 'Topogrofiner' by using field emission rather than tunneling in 1972. This instrument is very similar to the Scanning Tunneling Microscope. It has a sharp field emission tip scanned over the sample by means of piezoelectric translators. The field emission current is kept constant by adjusting the position of the tip during the scan. The resolution was approximately 1000Å in lateral direction. The topogrofiner can be thought as the ancestor of Scanning Tunneling Microscope.

Binnig, Rohrer and coworkers [8] have observed vacuum tunneling on platinum samples with tungsten tip and constructed the Scanning Tunneling Microscope [9] in 1982. In 1986, Binnig and Rohrer were awarded with the Nobel Prize in Physics for their construction of Scanning Tunneling Microscope.

Teague [10] and Poppe [11] have observed vacuum tunneling before Binnig and Rohrer. But their interest was not to use it in a microscope.

The underlying physical principle of the Scanning Tunneling Microscope (STM) is very simple, the electron tunneling.

A very sharp metallic tip is placed very close to a metal surface to form a vacuum tunnel junction. The tunneling current is a very sensitive function of barrier width. It approximately changes one order of magnitude for 1Å change in gap width. Therefore, most of the current is concentrated at the apex of the

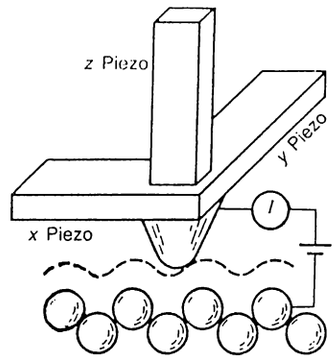

Figure 1.1. Schematic diagram of STM.

tip. This very fine current filament is scanned over the surface. The z-position of the tip is adjusted with a control circuit to keep the tunnel current constant as shown in Figure 1.1.

Therefore, z-position of the tip corresponds to constant current contour-plots. If the surface has uniform electronic properties (for example, free electron metals), then these contours corresponds to the topography of the surface. Since tunneling current also depends on surface densities of states, STM line scans have also information about local electronic properties of the surface. Therefore, it is possible to perform spectroscopy in atomic scale with STM. This method is called Spatially Resolved Spectroscopy or Scanning Tunneling Spectroscopy (STS) and successfully applied to semiconductors and superconductors.

Scanning Tunneling Microscope is a very local probe that can map the surface structures with atomic resolution. Surface structures have been studied by conventional electron microscopy (SEM, TEM, FIM), diffraction measurements (LEED, X-ray, He diffraction) and scattering (ion scattering) experiments. Although some of them give atomic resolution in very extreme conditions, direct imaging of surfaces with atomic resolution seemed to be impossible before the invention of STM. Figure 1.2 shows comparison between conventional microscopes and Scanning Tunneling Microscope.

Scanning Tunneling Microscope can image only metals or doped semiconductors. This can be thought as a limitation on the applications. However,

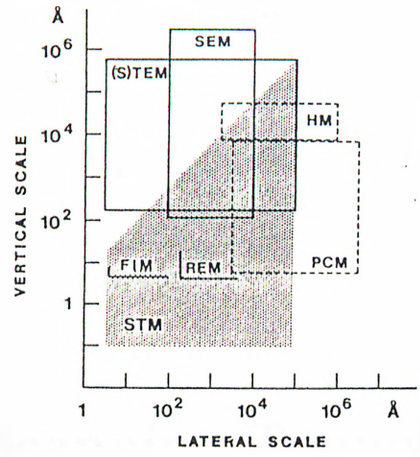

Figure 1.2. Comparison between microscopy techniques.

Lateral and depth resolution of several microscopes: scanning electron microscope (SEM), (scanning) transmission electron microscope ((S)TEM), high-resolution optical microscope (HM), field ion microscope (FIM), reflection electron microscope (REM), phase-contrast microscope (PCM) and scanning tunneling microscope (STM) (after Ref. [9]).

invention of the STM led to the development of wide variety of Scanning Probe Microscopes which will be discussed in Chapter 4. These techniques can be applied to almost any materials (insulators, optical materials, magnetic materials etc.) and open very fascinating opportunities in science and technology. Moreover, applications of the Scanning Tunneling Microscope has a very broad spectrum, extending from biology to chemistry. Development of STM has opened a new era in the surface science.

In this thesis, the construction of a Scanning Tunneling Microscope will be explained. In Chapter 2, theory of tunneling and Scanning Tunneling Microscope will be given. Instrumentation will be explained in Chapter 3. In Chapter 4, applications of the microscope and related techniques will be reviewed. Results obtained with the microscope will be presented in Chapter 5. Chapter 6 concludes the thesis.

Chapter 2

Theory of Scanning Tunneling Microscopy

Different methods have been developed to calculate the tunneling probability through a potential barrier since the birth of Quantum Mechanics.

The simplest model to describe tunneling between two systems separated in space is the one dimensional potential barrier. This model is treated in almost every Quantum Mechanics textbook and illustrated in Figure 2.1.

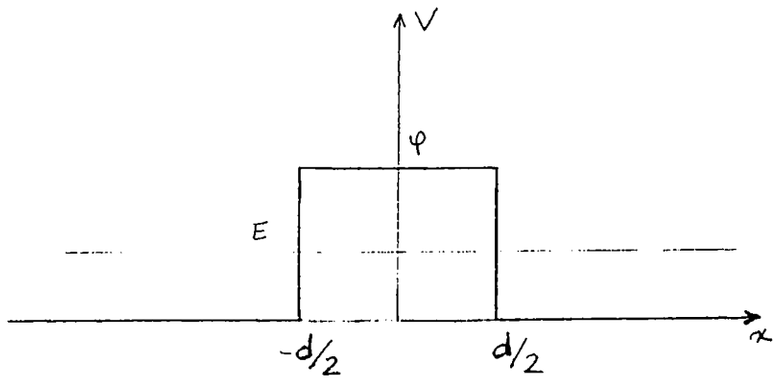

Figure 2.1. One dimensional potential barrier.

Although it is impossible for a particle to pass through the barrier classically, the particle can tunnel through the barrier with a finite probability. If the barrier is large and wide compared to characteristic quantities, the tunneling probability for a particle from left to right is given by

$$T \propto e^{-2\kappa d} \tag{2.1}$$

where d is the barrier width, and $\kappa = \frac{\sqrt{2m(\phi - E)}}{\hbar}$ is the inverse decay length of wavefunction in the barrier, ϕ and E being the barrier height and incident particle's energy, respectively.

Although the model is too simple to represent all the features of a tunnel junction, for example the one in STM, it gives the correct form of the tunneling probability as a function of gap distance.

In metals, electrons at the Fermi Level behave like free electrons with an associated effective mass. The work function, ϕ, is defined as the energy required to move an electron from Fermi level to the vacuum. Therefore One Dimensional Barrier model works quite well for the metal-insulator-metal tunnel junctions.

Simmons [12] has calculated the tunneling current density for two metal electrodes as

$$j = \frac{c}{d}\left[(\bar{\phi} - eV/2)e^{-A\sqrt{(\bar{\phi}-eV/2)}d} + (\bar{\phi} + eV/2)e^{-A\sqrt{(\bar{\phi}+eV/2)}d}\right] \tag{2.2}$$

where $\bar{\phi}$ is the average of the metal work functions and c is a constant. This expression is valid even for $V > \bar{\phi}$, Field Emission regime, and reduces to the following expression for small bias condition, $V \ll \bar{\phi}$;

$$\begin{aligned} j &= \frac{e^2}{\hbar}\frac{\kappa_0 V}{4\pi^2 d}e^{-2\kappa_0 d} \\ 2\kappa_0 &= 1.025\sqrt{\bar{\phi}}. \end{aligned} \tag{2.3}$$

2.1 Transfer Hamiltonian Method

Bardeen [13] has developed a general formalism for the theory of tunneling from many particle point of view. Although his theory is one dimensional, it can easily be generalized to three dimensions. He assumed two many-body systems separated by a barrier extending from x_a to x_b. Metal a is at the left of x_a and metal b is at the right of x_b. Then, he considered two many particle states of the whole system, ψ_0 and ψ_{mn}. ψ_{mn} differs from ψ_0 in that, only one electron is transferred from the state $|m>$ at a to the state $|n>$ at b.

Furthermore, ψ_0 and ψ_{mn} are assumed to be the solutions of the Schrödinger Equation in different regions,

$$\begin{aligned} \mathcal{H}\psi_0 &= E_0\psi_0 \qquad for \qquad x < x_b \\ \mathcal{H}\psi_{mn} &= E_{mn}\psi_{mn} \qquad for \qquad x > x_a \ . \end{aligned} \tag{2.4}$$

Therefore both wavefunctions are good solutions of the system in the barrier region. The time dependent wavefunction describing the system can be constructed with linear combination of ψ_0 and ψ_{mn} in a very similar way to the time dependent perturbation theory

$$\Psi(t) = a(t)e^{-iE_0t/\hbar}\psi_0 + \sum_{mn} b_{mn}(t)e^{-iE_{mn}t/\hbar}\psi_{mn} \ . \tag{2.5}$$

If we substitute the above equation to the time dependent Schrödinger's equation

$$\mathcal{H}\Psi(t) = i\hbar\frac{\partial}{\partial t}\Psi(t) \tag{2.6}$$

and carry out the algebra, we can find the time dependent probability amplitudes.

Since particles tunnel from state ψ_0 to ψ_{mn}, one can assume that $a(0) \simeq 1$, $b_{mn}(0) \simeq 0$ and $\frac{da}{dt}(0) \simeq 0$. These approximations give the following differential equation for the probability amplitude,

$$i\hbar\dot{b}_{mn}(t) = < \psi_{mn}|\mathcal{H} - E_0|\psi_0 > e^{-i\frac{E_{mn}-E_0}{\hbar}t} . \tag{2.7}$$

The above equation can be integrated easily and then the transition amplitude per unit time from state $|n> \rightarrow |m>$ is given by,

$$W_{mn} = \frac{2\pi}{\hbar}|M_{mn}|^2\delta(E_{mn} - E_0) \tag{2.8}$$

where $M_{mn} = < \psi_{mn}|\mathcal{H} - E_0|\psi_0 >$ is the transition matrix element. The delta function sifts only the energy conserving transitions. Since all the states having right energy contribute to the tunneling, the total tunneling current can be calculated as

$$I_t = \frac{2\pi e}{\hbar}\sum_{mn}|M_{mn}|^2\delta(E_{mn} - E_0) . \tag{2.9}$$

Therefore we can evaluate the tunneling current, if we calculate the transition matrix M_{mn}. Since ψ_0 is the eigenstate of the system for $x < x_b$, the integrand vanishes. Then, we can write for M_{mn}

$$M_{mn} = \int_b \psi^*_{mn}(\mathcal{H} - E_0)\psi_0 d\tau . \tag{2.10}$$

We can add $\psi^*_0(\mathcal{H} - E_{mn})\psi_{mn}$ to the integrand, because it is zero for the region b. Since we are only allowing energy conserving transitions, the relation simplifies further to

$$M_{mn} = \int_b (\psi^*_{mn}\mathcal{H}\psi_0 - \psi^*_0\mathcal{H}\psi_{mn})d\tau . \tag{2.11}$$

The potential energy does not contribute to the integral and we obtain

$$M_{mn} = -\frac{\hbar^2}{2m}\int_b (\psi^*_{mn}\nabla^2_x\psi_0 - \psi^*_0\nabla^2_x\psi_{mn})d\tau \ . \tag{2.12}$$

Integration by parts yields the following result,

$$M_{mn} = -i\hbar J_{mn}(x_1) \tag{2.13}$$

where $x_a < x_1 < x_b$ and

$$J_{mn}(x) = -\frac{i}{2m\hbar}(\psi^*_{mn}\nabla_x\psi_0 - \psi^*_0\nabla_x\psi_{mn}) \ . \tag{2.14}$$

This is the familiar current density operator in the Quantum Mechanics. The transition matrix is related to the current density operator evaluated at x_1, somewhere inside the barrier.

Bardeen's formalism is very similar to time dependent perturbation theory, but it uses an overcomplete basis set for the expansion, because ψ_0 and ψ_{mn} are good solutions of Schrödinger's Equation in the barrier region. The Eqn 2.9 is Fermi Golden Rule type expression for the total tunneling current.

Bardeen's formalism is quite powerful , because it can be used to calculate tunneling current for any system, for example superconductor-normal metal junctions, tunnel diode, STM etc. On the other hand, calculation of current density operator, J_{mn}, is very difficult for most of the systems and requires further approximations. His theory is the starting point of the most of the tunneling calculations.

2.2 Tersoff–Hamann Theory

The most successful theory of STM was developed by Tersoff and Hamann [14] in 1983. They applied Bardeen's formalism to STM by modeling the tip with a metal sphere.

If the statistical factors are included in the Bardeen's result (Eqn. 2.9), one can write

$$I_t = \frac{2\pi e}{\hbar} \sum_{\mu\nu} f(E_\mu)[1 - f(E_\nu + eV)] \times |M_{\mu\nu}|^2 \delta(E_\mu - E_\nu) \tag{2.15}$$

where $f(E)$, V, ψ_μ and ψ_ν are Fermi–Dirac distribution function, bias voltage, tip and surface states, respectively.

For low bias condition, $V \simeq 10mV$, which is a typical value in STM experiments, the expression reduces to

$$I_t = \frac{2\pi e}{\hbar} \sum_{\mu\nu} |M_{\mu\nu}|^2 \delta(E_\nu - E_F)\delta(E_\mu - E_F) \tag{2.16}$$

where E_F is the Fermi level for the metals.

Generalization of the Bardeen's formalism to three dimensions gives

$$M_{\mu\nu} = -\frac{\hbar^2}{2m} \int d\vec{s} \cdot (\psi_\mu^* \vec{\nabla} \psi_\nu - \psi_\nu^* \vec{\nabla} \psi_\mu) \ . \tag{2.17}$$

The surface integral must be calculated at the boundary of the barrier.

They expanded the surface wavefunction into a very general form to calculate the matrix elements $M_{\mu\nu}$ as

$$\psi_\nu = \frac{1}{\Omega_s} \sum_{\vec{G}} a_{\vec{G}} exp\left\{-(k_2 + |\vec{k}_{||} + \vec{G}|)z\right\} exp\left\{i(\vec{k}_{||} + \vec{G}) \cdot \vec{x}\right\} \tag{2.18}$$

where Ω_s, $k = \frac{\sqrt{2m\phi}}{\hbar}$ and $\vec{k}_{||}$ are surface volume, inverse decay length of the surface wavefunction and surface Bloch wavevector, respectively.

On the other hand, the tip wavefunction is assumed to have asymptotically spherical form

$$\psi_\mu = \frac{1}{\Omega_t} c_t k R e^{kR} \frac{e^{-k|\vec{r}-\vec{r}_0|}}{|k(\vec{r}-\vec{r}_0)|} \tag{2.19}$$

where R, $\vec{r}_0$, Ω_t and c_t are radius of curvature, position of the center, volume of the tip and a normalization constant, respectively.

If these wavefunctions are inserted in Eq. 2.17, the transition matrix can be found as

$$M_{\mu\nu} = \frac{\hbar^2}{2m} \frac{1}{\Omega_t} k R e^{kR} \psi_\nu(\vec{r}_0) \ . \tag{2.20}$$

The tunneling current is then

$$I = 32 \frac{\pi^3}{\hbar} e^2 \phi^2 V \mathcal{D}_t(E_F) e^{2kR} \times \sum_\nu |\psi_\nu(\vec{r}_0)|^2 \delta(E_\nu - E_F) \tag{2.21}$$

where $\mathcal{D}_t(E_F)$ is density of states at the Fermi level at the tip.

The tunneling conductance, σ_t is

$$\sigma_t \propto \rho(\vec{r}_0, E_F) \tag{2.22}$$

where

$$\rho(\vec{r}, E) = \sum_\nu |\psi_\nu(\vec{r})|^2 \delta(E_\nu - E) \tag{2.23}$$

is density of states at position $\vec{r}$ and the energy E, for the surface.

Therefore, if the shape of the tip does not change during the experiment and the gap distance is large, the STM contourplots correspond to the charge density corrugation at the Fermi level. They made use of the independent electrode approximation which makes their theory valid for large tip–sample separations.

Tersoff and Hamann applied their theory to Au(110) (1×2) and (1×3) reconstructed surfaces. Their results were in very well aggrement with the experiment.

However, their theory is not valid for small tip–sample separations, the spherical tip approximation also causes some artifacts.

2.3 Other Methods

Garcia *et al.* [15] and Stoll *et al.* [16] have directly solved the Schrödinger equation to calculate the tunnel current. They assumed different periodic model potentials for the tip and the sample. The tip potential period was kept large enough to decouple the neighboring tips. They have found very similar expression for the tunneling current. They have applied their theories to Au(110) (1×2) reconstructed surface and obtained successful results.

As the tip approaches towards the sample, they start to interact with each other. If the tip is brought very near to the sample, the interaction becomes very strong and must be included in the calculations.

Tunneling probability can not be calculated by Tersoff–Hamann theory, because the electrodes are now very strongly interacting with each other. A new method should be developed.

Tekman [17] introduced the concept of Tip Induced Localized States (TILS), the states that appear between tip and sample for very small tip–sample distances. They modified the Bardeen's formalism to include the tunneling through the Tip Induced Localized States and calculated the tunneling current at various tip positions for graphite. He found an enhancement in the corrugation amplitude of a factor > 4.

Çıracı [18] *et al.* have carried out *ab initio* total energy, force and electronic structure calculations for tip–sample interactions. They have used graphite monolayer and 2×2 array Aluminum tip atom for their calculation. They

have found that a dramatic change in the electronic structure at small tip–sample separations. At this regime, local density of states changes drastically and new tunneling matrix elements must be calculated to find the tunneling current.

Chapter 3

Instrumentation

Three dimensional variations in the surface charge density are probed using electron tunneling in Scanning Tunneling Microscopy. Figure 3.1 shows schematic diagram of a Scanning Tunneling Microscope. When a bias voltage is applied between tip and sample, electrons start to tunnel through the vacuum gap, which is typically 10Å. A feedback loop controls the tunnel gap by adjusting the z-position of the tip and maintains a constant tunneling current. The tip is scanned over the surface by x-y piezo translators, change in the z-position of the tip corresponds to the topography of the surface. This configuration is called *constant current mode.*

The tip can be scanned at constant z-position and variation in the tunneling current resulting from the surface topography can be recorded. This mode is called *constant height mode.* This mode is faster than the constant current mode, but the surfaces must be smooth to avoid tip crashing.

Important design criteria and instrumentation details are described in this chapter.

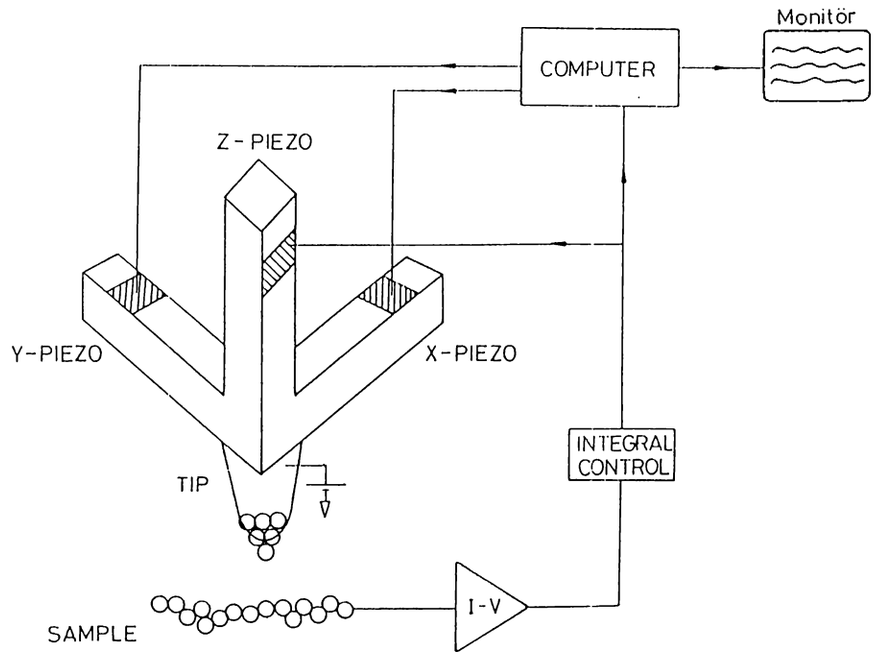

Figure 3.1. Schematic diagram of STM.

3.1 Vibration Isolation

The tunneling current depends exponentially on the gap distance variations. This dependence enables us to build a very powerful microscope, the STM. On the other hand, this dependence makes the microscope very sensitive to the external disturbances. Typical corrugation amplitudes measured in constant current mode is of the order of 0.1 Å. Therefore external vibrations coming from the laboratory floor must be damped down to an amplitude of 0.01 Å or less. This is one of the most important instrumentation problems we have faced while we were constructing the STM.

Vibrations exist mainly at 17,25 and 50 Hz due to motors and transformers that are placed in almost every building. Vibration isolation systems for STM were extensively studied by several authors[19, 20].

Magnetic levitation was used to isolate the first STM from external

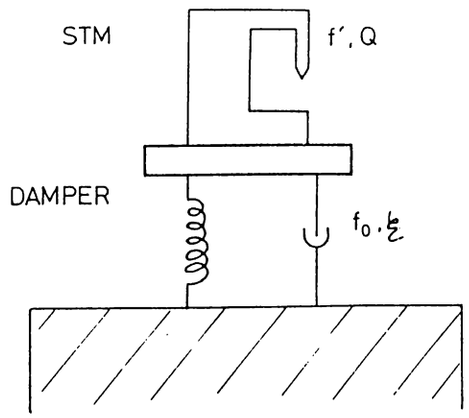

Figure 3.2. Simplified model for Vibration Isolation System.

vibrations[8]. Later, single or double stage spring systems with eddy current damping mechanism were commonly used. In these systems [19], STM is suspended by using metal springs. The vibrations are damped by magnets which induce eddy currents in the metal plates that are placed close to the magnets.

Simplified schematic of a single stage vibration isolation system and STM is shown in Figure 3.2.

Vibrations coming from the laboratory floor is transmitted to the STM stage with a transfer function [19]

$$T = \left(\frac{1 + (2\xi f/f_0)^2}{(1 - f^2/f_0^2)^2 + (2\xi f/f_0)^2} \right)^{1/2} \tag{3.1}$$

where f_0 is the resonant frequency and $\xi = \gamma/\gamma_c$, ($\gamma_c = 4m\pi f_0$, critical damping coefficient) is the damping ratio of the system. The transfer function is plotted for various ξ in Figure 3.3. The resonant frequency should be kept as low as possible to obtain high attenuation. Attenuation is large for small ξ, but resonance amplitude is also larger. On the other hand, we can not increase ξ very much, because attenuation drops. Therefore we should set ξ to something between 0.1–0.3. Since eddy current damping is usually used, ξ can be adjusted by changing magnets' position and size.

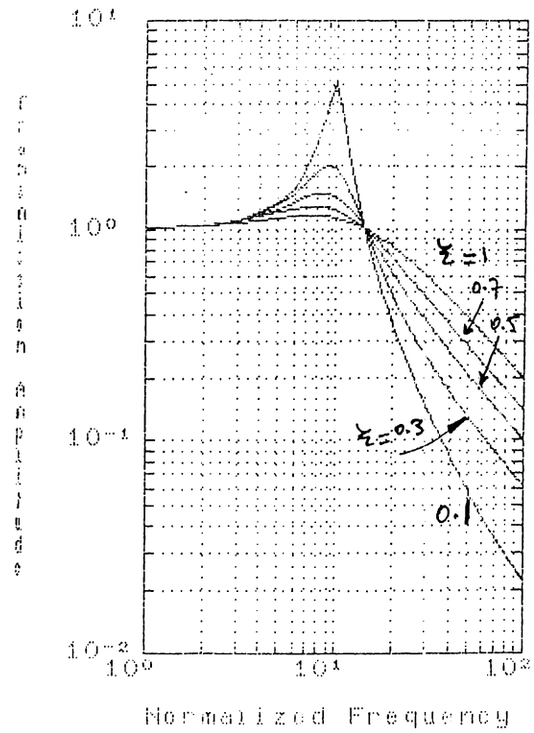

Figure 3.3. Transfer function for single stage Vibration Isolation System.

Rubber can also be used instead of metal springs in vibration isolation systems. Four or five stainless steel plates separated by small viton pieces are used for this purpose in Pocket Size STM[21]. The viton is used for its Ultra High Vacuum (UHV) compatibility. But these systems have rather low (>10Hz) resonant frequency compared to the spring systems.

Commercial vibration isolation systems can also be used to support STM. Pneumatic springs are used to suspend a large mass. These systems have usually very low resonant frequency (typically 1 Hz), and adjustable ξ resulting in a very good attenuation.

Moreover, the STM has structural damping. The vibrations are dissipated by hysteresis loss due to structural damping of the rigid body. STM can be modeled by a second order system. The transfer function is given by [20]

$$T_s = \frac{(f/f_s)^2}{[(1 - f^2/f_s^2)^2 + (f/Qf_s)^2]^{1/2}} \tag{3.2}$$

where f_s and Q are resonance frequency and quality factor of the tunnel junction. Therefore rigidly constructed STM, which has high resonance frequency, does not require vibration isolation[22].

If $f_s \gg f_0$ then the transfer function of the whole system is given by[20]

$$T_{tot} = \left(\frac{1 + (2\xi f/f_0)^2}{(1 - f^2/f_0^2)^2 + (2\xi f/f_0)^2} \right)^{1/2} \times \frac{(f/f_s)^2}{((1 - f^2/f_s^2)^2 + (f/Qf_s)^2)^{1/2}} \ . \quad (3.3)$$

Our system is similar to Pocket Size STM [21]. We stacked five brass plates separated by rubber pieces cut from an O-ring. A marble block , which weighs $\sim$ 70 kg, is placed on two bicycle tires. A concrete block which sits on a smaller tire is put on the marble block. STM is put on this concrete block. The whole system is on a table whose legs are standing on the sand pool.

3.2 Mechanical Design of STM

There are several criteria to be satisfied to construct an ideal STM. The tip could be scanned over the sample in the range of $\sim 1\mu m$ in x-y direction with a resolution of 0.1 Å, and in the range of $\sim 1\mu m$ in z direction with resolution of 0.01 Å. The scanner should have high mechanical resonance frequency and low Q to obtain sufficient isolation from disturbances and fast operation of STM.

A coarse approach mechanism must be capable of positioning the sample within the scanner's range in a reliable manner. There must be several steps of sample positioner in the range of the scanner. Furthermore, the whole system should be as rigid and compact as possible in order not to reduce the mechanical resonance frequency of STM.

Our instrument is shown in Figure 3.4. We have constructed a tripod scanner for tip positioning and a step motor for sample approach. Five brass plates separated by rubber pieces are used for vibration isolation.

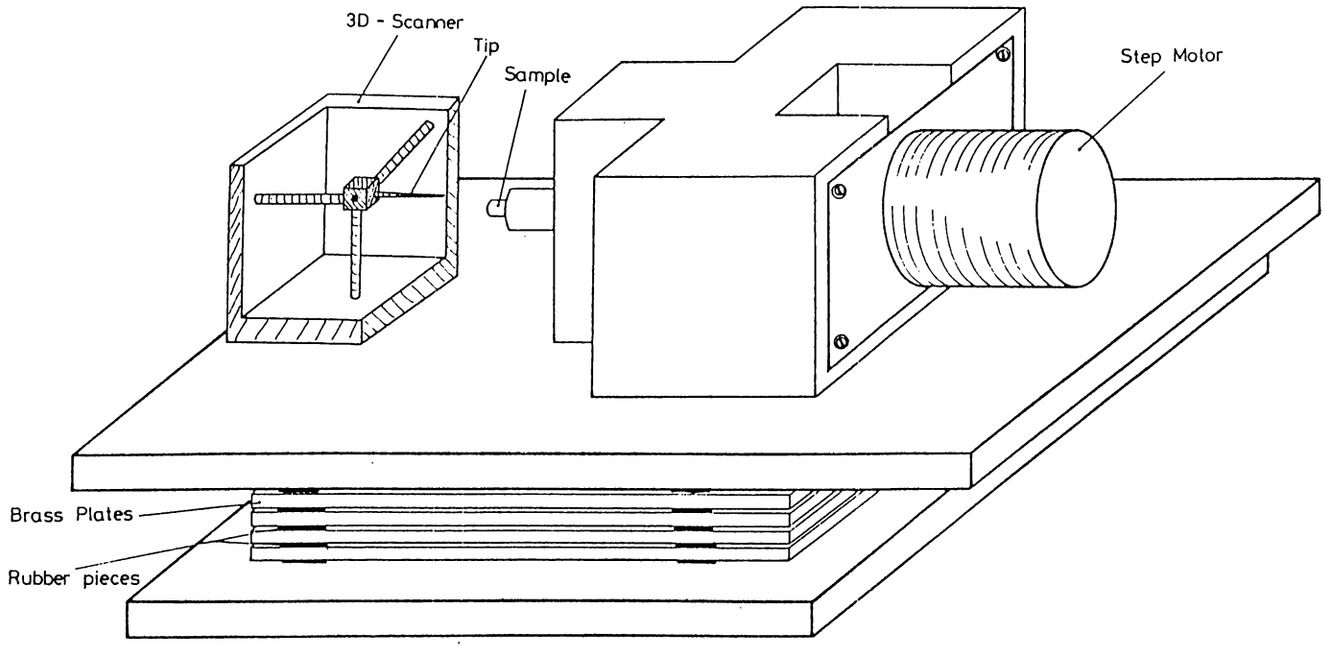

Figure 3.4. Scanning Tunneling Microscope.

3.2.1 Coarse Approach Unit

Different sample approach mechanisms have been developed for STM by various groups. The electrostaticaly clamped louse [9] was the first. It has a piezoelectric ceramic body standing on three metal feet which stand on a metal baseplate. The feet are isolated from the baseplate by a very thin insulator. The feet can be independently clamped to baseplate by applying voltage between the baseplate and the feet. The louse moves forward by clamping the back foot and elongating piezo body. Then, front feet are clamped, back foot is unclamped and piezo is contracted to complete a step. Step sizes of 10-1000 Åand speeds of up to 1000 step/s can be attainable.

Mechanically clamped inchworm [23], magnetically driven micropositoner [24, 30], manually [25] or motor [26, 27] driven differential micrometer, differential spring adjuster [25] and inertial slider [28] have also been reported

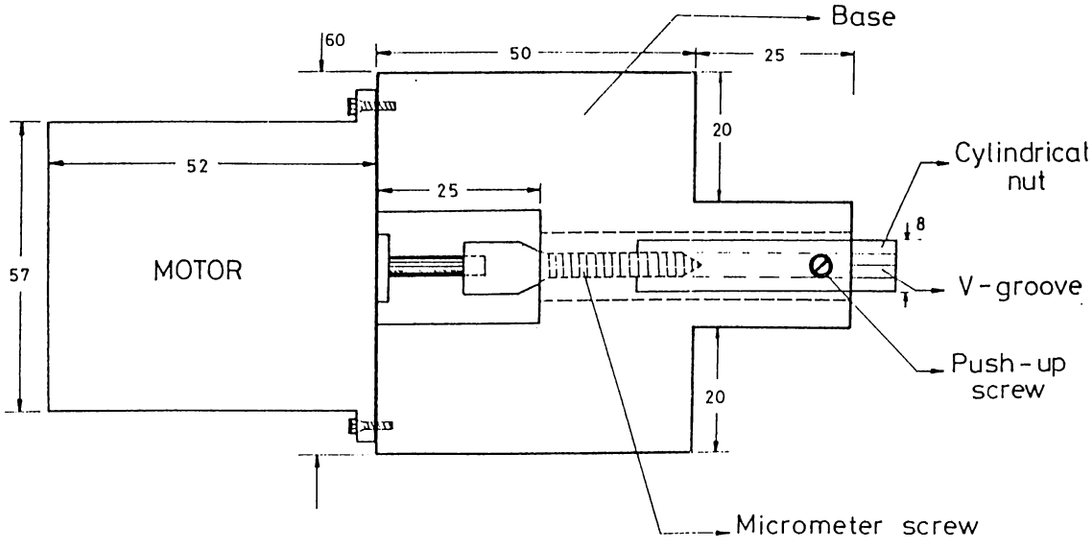

Figure 3.5. A micrometer screw driven by a step motor.

for sample approach systems. Each system has a different drawback. Electrostatic louse often sticks to the baseplate and doesn't move at all. Magnetically driven micropositoner causes thermal drift during the operation. Manually driven differential micrometer couples vibrations during sample approach. However almost , every design works.

We have observed the first tunneling in an apparatus having manually driven micrometer with a lever reduction system for coarse positioning and a tube z-scanner with a sewing needle attached onto it. Vibrational coupling during the sample approach forced us to continue with another scheme. We, then tested electrostatic louse, but failed. However, our last design, a micrometer driven by a step motor as shown in Figure 3.5 , works quite well.

A micrometer screw which drives a cylindirical nut is directly coupled to the rotor. The nut has a v-groove on its side along the axis, and it is free to move in a cylindrical hole formed in the body. Rotation of nut in hole is inhibited by pushing v-groove with a ball loaded by a spring.Therefore, rotation of the motor moves the nut, along the z axis. A teflon isolator is fitted tightly at the end of the nut and the sample holder can be inserted firmly into a hole in the teflon isolator.

The micrometer screw has threads of 2 pitch/mm and motor has 1.8^0 steps (200 steps/rev). Therefore, each motor step corresponds to a $2.5\mu m$ movement of sample. This is four times larger than the range of the z-scanner. We have reduced the step size of the positioner by making use of microstepping technique. Microstepping is a common trick to increase the resolution of the step motors. Our motor is a two phase step motor. If we apply $I_0 sin(\omega t)$ to one of the phase and $I_0 cos(\omega t)$ to the other, motor rotates with constant speed. If we discretize those signals, then motor makes steps. The normal stepping is to discretize the sinusoidal current signals in three levels: $-I_0, 0, I_0$. Therefore if we divide the period of the sine wave into smaller pieces, it makes smaller steps, i.e. microsteps. If the motor is machined precisely then the limiting factor is the driving electronics. One can make as many microsteps as he or she wishes. Our motor driving electronics, shown in Figure 3.6, processes the signals coming from computer and drives the coils of motor with predetermined current values. The desired signal is generated by two independent DACs in the data acquisition card [29] with a short subroutine. We can easily change number of microsteps within the software. We have achieved up to 200 microsteps with an unloaded motor. But when we load the motor by the nut , maximum number drops to 100. The smaller microsteps becomes unreliable. We have measured the size of microsteps with a Michelson Interferometer whose movable mirror is mounted on the sample holder which loaded the motor. For unloaded one, we have glued a mirror on the spindle and reflect a laser beam from that. The reflected beam is directed on the wall which is 4 m away from the mirror. Therefore small rotations of the spindle can be easily measured.

Very recently, we have constructed a magnetically driven sample positioner [24], which will be described in detail elsewhere [30]. A small permanent magnet having three steel ball bearings at the bottom, stands on a microscope slide. A coil is placed under the slide. Application of pulsed currents to the coil exerts inertial jerks to the magnet on which the sample is mounted. Due to frictional forces the sample holder moves little bit and stops. Step size can be adjusted with the pulse duration. Steps as small as 5 nm are reproducible.

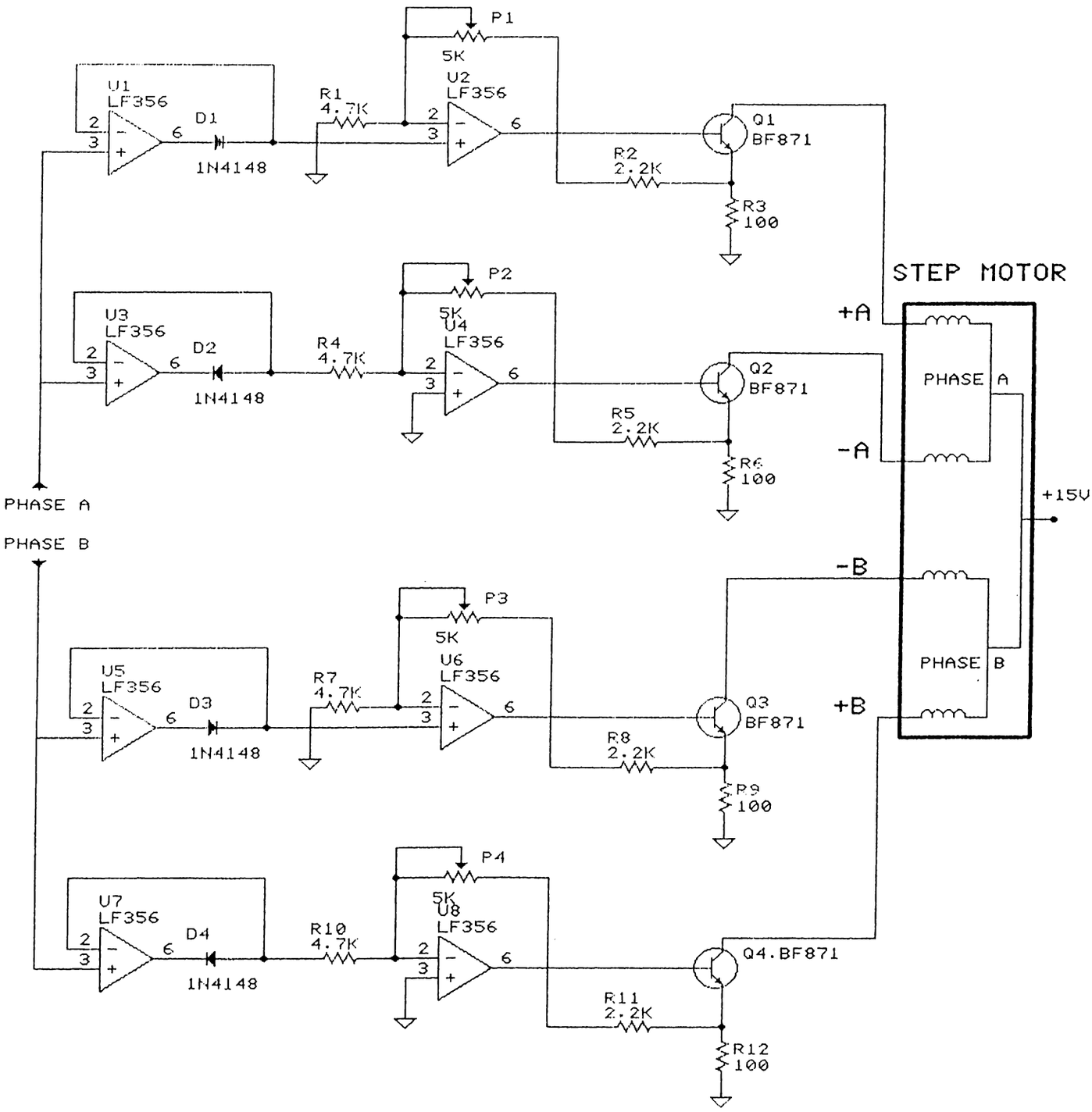

Figure 3.6. Motor Drive Circuit.

3.2.2 Scanner

The scanner is used to move the tip across the surface and to adjust the tunneling gap. Piezoelectric materials in various shapes are widely used for this

purpose. Important criteria for a high performance scanner can be summarized as follows:

- High Resolution : ~ 0.1 Å in z direction, ~ 1 Å in x & y direction.
- Large Scan Area : $\sim 1\mu$m in all directions.
- Rigidity : necessary, for fast operation and immunity to disturbances.
- Cross Coupling : motion in one axis should not affect the others.
- Linearity : the motion of the scanner should be linear throughout its range.

Piezo bars attached in tripod form was the first STM scanner used by Binnig and Rohrer [9]. Wide variety of scanners have been developed by other groups. Bimorph driven tripod [31] in which circular bimorph elements drive an aluminum tripod, small piezo cubes assembled in matrix form to reduce the thermal drift [32], the popular single tube scanner developed by Binnig and Smith [35] and microscopic scanner in single chip STM [33], to name a few.

The single tube scanner is very small and rigid, therefore has resonant

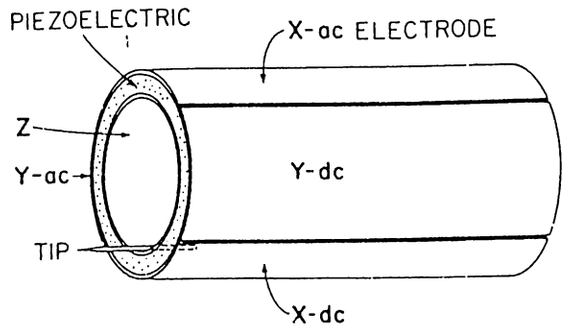

Figure 3.7. Single Tube Scanner

frequencies as high as 8 KHz. Outer electrode of a piezo tube is separated into four equal parts parallel to its axis as shown in Figure 3.7. The tube is mounted from its base. Elongation and contraction of one of the quadrants bends the end of the tube at which the tip is placed. Therefore tip can be scanned over the surface by applying appropriate voltages to the appropriate quadrants. Common electrode inside the tube can be used for z motion. Alternatively, z-voltage can be added to the quadrants. If the tip is mounted symmetrically for thermal drift compensation in x&y directions, symmetrical voltages should be applied to the opposing quadrants. Since single tube scanner is very simple and robust, it is very popular.

Our scanner is constructed using small piezo tubes [34] which are glued in tripod form to an aluminum base and a $(1 \times 1 \times 1)$ cm aluminum junction as shown in Figure 3.8. Tubes are 20 mm long with 3 mm OD and 2 mm ID. A tip holder is clamped by a set screw to the junction. Outer electrodes are connected to the scanner base with conductive epoxy. Electrical connections to the tubes are also made by conductive epoxy and a Molex type connector mounted to the scanner base. The scanner body is mounted to the base of the microscope with two screws. Hence, scanner unit can be easily disconnected from the base.

Although the tubes are expected to be identical, the tube's sensitivities are measured by Michelson Interferometer as follows:

$$x : 45 \mp 10\% \ \frac{\mathring{A}}{V}$$

$$y : 33 \mp 10\% \ \frac{\mathring{A}}{V}$$

$$z : 25 \mp 10\% \ \frac{\mathring{A}}{V} \ .$$

Our range is about 6000 Å with peak to peak voltage of 250 V from the output of high voltage amplifiers designed and implemented for this purpose. Since we usually keep the scanning range less than 100 Å, hysteresis and creep do not cause any problem for most of the cases.

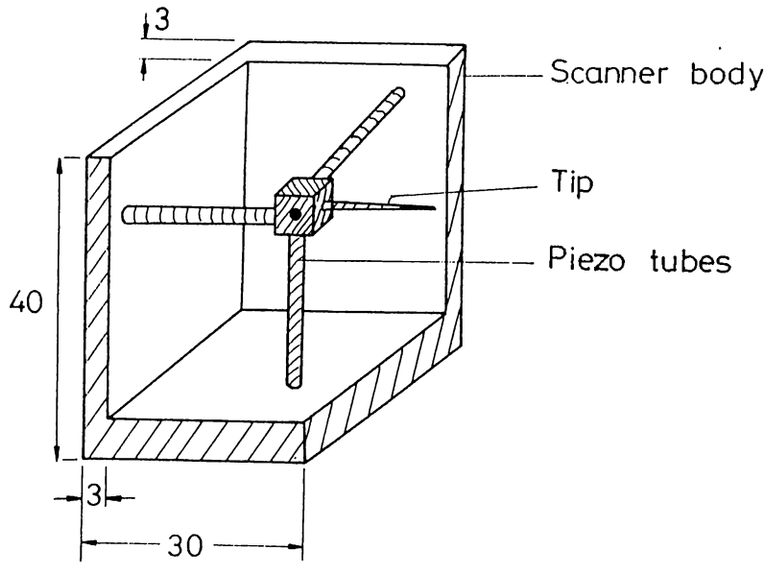

Figure 3.8. Scanner Unit

3.2.3 Tip

The tip is the most critical part of the STM that directly determines the resolution. Tips are usually prepared from metal wires. Very sharp tips, usually single atom tips are necessary to obtain atomic resolution. On the other hand, quite dull tips must be used for Scanning Tunneling Spectroscopy because of Heisenberg's uncertainty principle:

$$\Delta k \Delta x \geq 1 \tag{3.4}$$

If the tip is sharp (i.e. Δx is small) then Δk is large. Therefore momentum, hence energy resolution of the tip is poor.

Although the radius of curvature of the tip may be quite large, a single atom sitting at the apex of the tip works as a very sharp tip. STM images are very closely related to the atomic structure of the tip. This dependence was predicted [36] and observed by different groups. Park *et al.* [37] have observed multiple tip effects on graphite sample. Kuk and Silverman have investigated for the first time how atomic structure of the tip affects STM images [38].

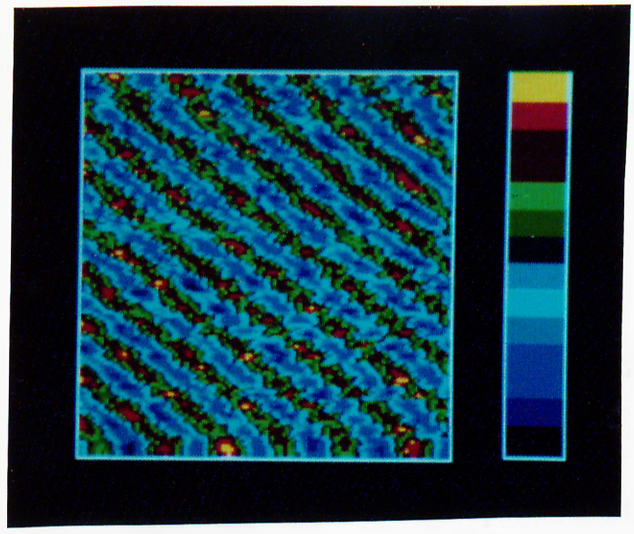

Figure 3.9. Effect of multiple atoms at the apex of the tip

Constant height image of graphite surface. The image is approximately 14×18 $\AA^2$.

They have determined the tip structure *in situ* by Field Ion Microscope before using it in STM. We have also observed this effect on graphite. Due to two (or more) atoms at the apex, only rows of carbon atoms on the graphite surface are resolved as shown in Figure 3.9. Another image taken with the same tip after 5-10 minutes, is shown in Figure 3.21. This atomic resolution picture is most probably due to presence of a single atom at the apex.

Various metals, such as Tungsten, Gold, Platinum and even Graphite [39], can be used as a tip after sharpening properly. Electrochemical etching, borrowed from Field Ion Microscopy studies, has been used widely to form STM tips. Another method to produce good tips is to cut a Pt wire with an angle to its axis. A tungsten wire is immersed 4–5 mm into 1 M NaOH solution while the other electrode, which has circular form, is placed at the bottom of the cell. 10–20 V_{ac} is applied between electrodes as shown in Figure 3.10. The applied voltage or concentration of electrolyte are not so critical and only determine the speed of etching. Sharpness of tip depends on the tip's initial shape and the length of the immersed part. Sharpness is controlled with a $\times 240$ optical microscope. The process is stopped when no finite radius can

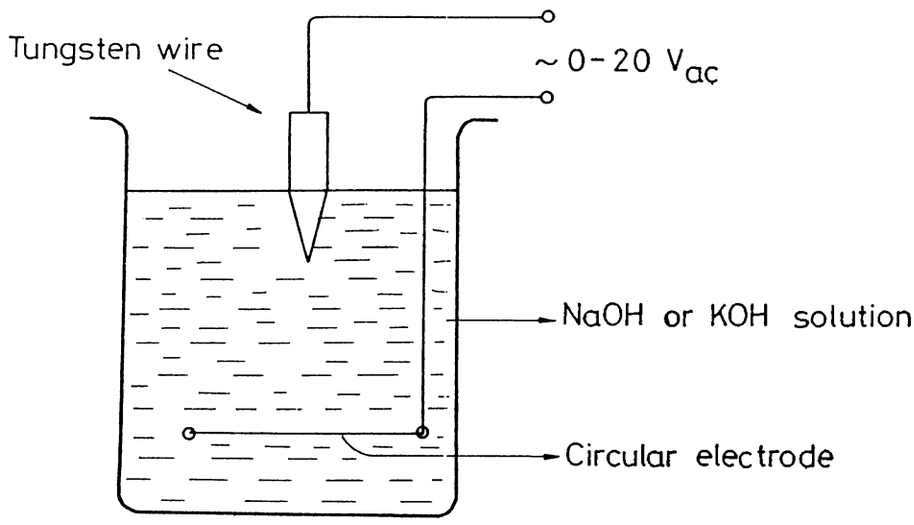

Figure 3.10. Tip etching

be observed with the microscope. Tips produced by this method usually have some oxide layers at the surface therefore, some of them do not give atomic resolution. Ion Milling has been proposed to remove the oxide layer[40]. Most of the tips are reported to give atomic resolution after this process.

Tip fabrication is not very controllable. We can't be sure which tip will give atomic resolution. Sometimes a fresh etched tip doesn't work, but one day later one can resolve the Carbon atoms on Graphite surface with the same tip! STM tips are also not very stable. The tips can suddenly deform or reform and obtained image becomes poorer or better! There are some methods to clean deformed tips. We sometimes tap the marble block on which STM sits to achieve atomic resolution while it is running. Field Emission from tip with ~ 100 V , a short voltage pulse to tip bias, letting it to scan for a long time are reported as a useful techniques for *in situ* tip cleaning [41].

State of the art tip fabrication has been done by Fink [42]. He uses Field Ion Microscope to stick different atoms to the apex to produce very stable mono atomic tips. Those tips are used to generate monochromatic and focused electron beams.

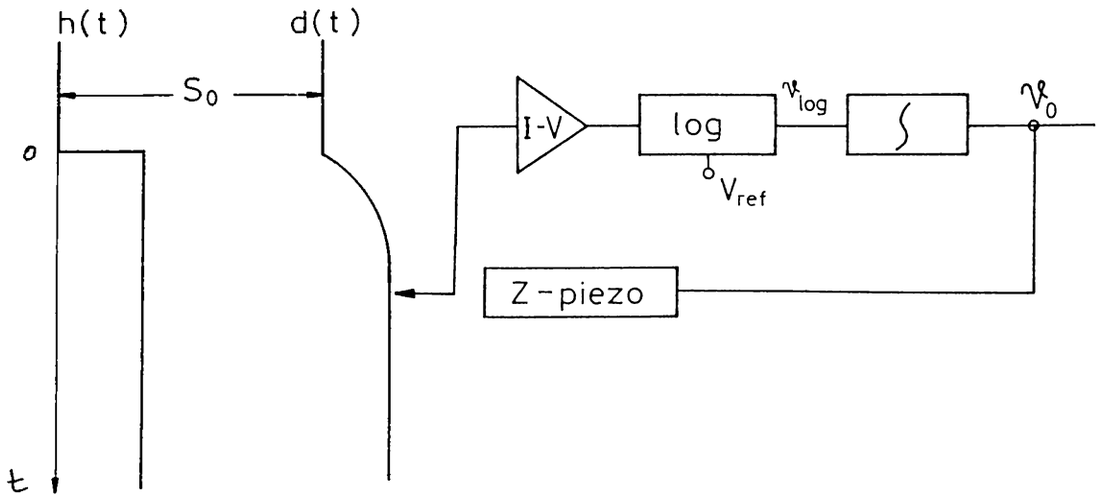

Figure 3.11. Simplified STM control circuit.

3.3 The Control System

The simplified block diagram of the STM control system is shown in Figure 3.11. The tunneling current is converted to voltage, then linearized and compared with a reference current level by a logarithmic amplifier. Then, the resulting signal is amplified and integrated. This signal is applied to the z–piezo to regulate the tunnel gap.

In the constant current mode, the tip is scanned over the surface. Since the equilibrium gap changes due to surface corrugation, the tunneling current also changes. The control circuit should move the tip to establish the equilibrium tunnel gap.

Since we scan the tip over the sample, it is more appropriate to describe the surface corrugation as a function of time, $h(t)$. The position of the tip, $d(t)$, is measured from the equilibrium gap , s_0, as shown in Figure 3.11. Therefore change in the gap distance is

$$\Delta s(t) = d(t) - h(t) \; . \tag{3.5}$$

The tunneling current is then

$$I(t) = I_0(s_0)e^{-\beta\Delta s(t)} \tag{3.6}$$

where $I_0(s_0)$ is the reference current and β is the inverse decay length of the wavefunction in the barrier. The gain of the I–V converter , a V/A, only effects the equilibrium tunneling current and does not contribute to the loop gain. The gain and the reference level of the logarithmic amplifier is adjusted such that the output of the log amp is

$$v_{log}(t) = -b\, s(t) \ . \tag{3.7}$$

Therefore, we measure the change in the gap at the output of the logarithmic amplifier. The output of the integrator, which follows the logarithmic amplifier is

$$v_o(t) = \frac{1}{RC}\int_0^t v_{log}(\tau)d\tau \tag{3.8}$$

where RC is the time constant of the integrator. The output voltage, which is applied to z–piezo is

$$v_o(t) = -\frac{bd}{RC}\int_0^t \Delta s(\tau)d\tau \ , \tag{3.9}$$

$$v_o(t) = -\frac{bd}{RC}\int_0^t [d(\tau) - h(\tau)]d\tau \ . \tag{3.10}$$

If we take time derivative of the above equation, we obtain

$$\frac{d}{dt}v_o(t) = -\frac{bd}{RC}d(t) + \frac{bd}{RC}h(t) \ . \tag{3.11}$$

This is the differential equation that relates the output to the input of the system.

The position of the tip, $d(t)$, which is the output of the transducer, is related to the input of the transducer, $v_o(t)$. This relation is quite complicated and can be described by the following convolution integral

$$d(t) = \int_{-\infty}^{+\infty} v_o(\tau)k(t-\tau)d\tau \tag{3.12}$$

where $k(t)$ is the impulse response of the transducer. Then, Eq. 3.13 becomes

$$\frac{d}{dt}v_o(t) = -\frac{bd}{RC}\int_{-\infty}^{+\infty} v_o(\tau)k(t-\tau)d\tau + \frac{bd}{RC}h(t)\ . \tag{3.13}$$

Since an electromechanical transducer has infinite number of modes, the exact response of the transducer is quite complicated. Park and Quate [19] modeled the transducer with a delayed system

$$d(t) = kv_{in}(t-\tau) \tag{3.14}$$

where $v_{in}(t)$, k and τ are the input voltage, gain and delay time of the transducer, respectively. This approximation which ignores the resonant behavior of the transducer does not simplify, indeed complicates the necessary algebra. Because, a delayed differential equation must be solved for stability analysis.

The transducer can be modeled with a second order system quite accurately. In fact, our approach includes the previous one. Because, step response of a second order system has some delay. The Laplace transform of the $k(t)$ is then,

$$K(s) = \frac{k\omega_0^2}{s^2 + 2\alpha s + \omega_0^2} \tag{3.15}$$

where ω_0, α and k are the resonance frequency damping factor and the gain of the piezo transducer, respectively. α is related to the quality factor, Q, of the piezo as follows

$$\alpha = \frac{\omega_0}{2Q} \ . \tag{3.16}$$

If we take Laplace transform of Eq. 3.17, we obtain

$$sV_o(s) = -\frac{bd}{RC}V_o(s)K(s) + \frac{bd}{RC}H(s) \tag{3.17}$$

where $V_o(s)$ and $H(s)$ are the Laplace transforms of $v_o(t)$ and $h(t)$, respectively.

Output of the system can be found as a function of the input

$$V_o(s) = \frac{bd/RCs}{1 + (bd/RCs)K(s)}H(s) \ . \tag{3.18}$$

If we define $G(s)$ as

$$G(s) = \frac{bd}{RCs} = \frac{\gamma}{s} \ , \tag{3.19}$$

then, Eq. 3.18 becomes

$$V_o(s) = \frac{G(s)}{1 + G(s)K(s)}H(s) \ . \tag{3.20}$$

The transfer function of the closed loop system is simply

$$T(s) = \frac{G(s)}{1 + G(s)K(s)} \ . \tag{3.21}$$

The block diagram of the closed loop system is given in Figure 3.12. This is a typical feedback system that can be analyzed with standard control engineering tools [43]. The gain of the system, γ, should be large for fast operation of the feedback loop. On the other hand, gain can not be increased indefinitely,

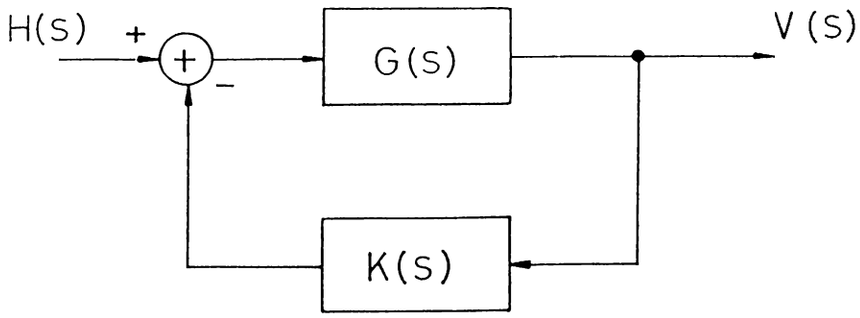

Figure 3.12. Block diagram of the Feedback System.

because the system starts to oscillate. Therefore the maximum allowable gain should be determined as a function of system parameters.

If the poles of the $T(s)$ are in complex right–half plane then the system is unstable. Position of the poles of $T(s)$, which is identical to the position of zeros of the denominator of $T(s)$ on the complex s–plane, is plotted in Figure 3.13 for different gain values. The arrows show the movement of the poles as the loop gain increases. This method is called the *Root–Locus Method* [43].

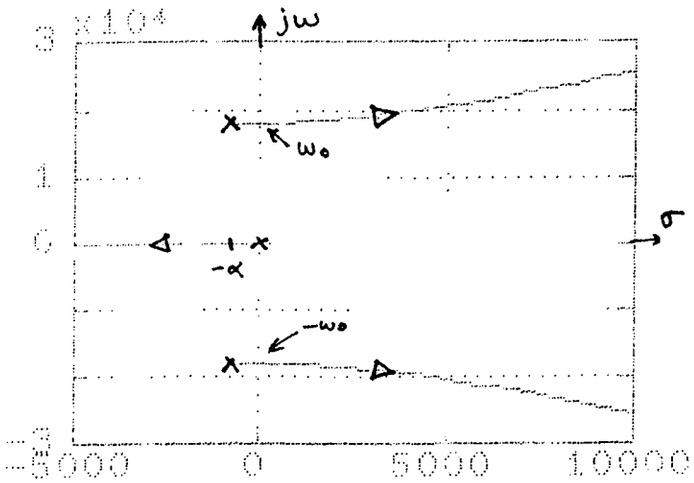

Figure 3.13. Root–Locus plot of $T(s)$.

The maximum allowable loop gain is calculated to be

$$g_{max} = \gamma_{max} k = \frac{\omega_0}{Q} \, . \tag{3.22}$$

The system starts to oscillate with frequency ω_0 at this gain. The critical part of the system that limits the gain is the transducer. We need large ω_0 and low Q for high performance. The performance of the system can be increased by lowering the Q of the system by potting the piezo scanner [44].

Our scanner's specs are as follows

- $k = 25$ Å/V
- $\omega_0 = 1.8 \times 10^4 \; rad/s$
- $Q \sim 10$

3.4 Electronics and Computer Interface

The block diagram of the STM electronics is given in Figure 3.14. A bias voltage is applied to the tip and the tunneling current is measured from the sample. The scan signals are generated by two DACs under the computer control. The rough approach is controlled with a step motor driver described in previous sections.

The whole system is accessible with a **DT2821–F** data acquisition card [29] plugged in a PC/AT compatible computer. DT2821–F has two 12–bit DACs, an 8–channel multiplexed 12–bit differential ADC (Analog to Digital Converter) and a 16–bit Digital I/O. DACs and ADC can be clocked up to 200 KHz and 150 KHz, respectively.

Step motor approaches the sample to the tip. Tip is retracted before each step to avoid crashing into the surface. After a step is completed, the tip is released. If the tunneling current is detected, then program takes care that the tip would stay within the z–scanner's range by moving the sample back and

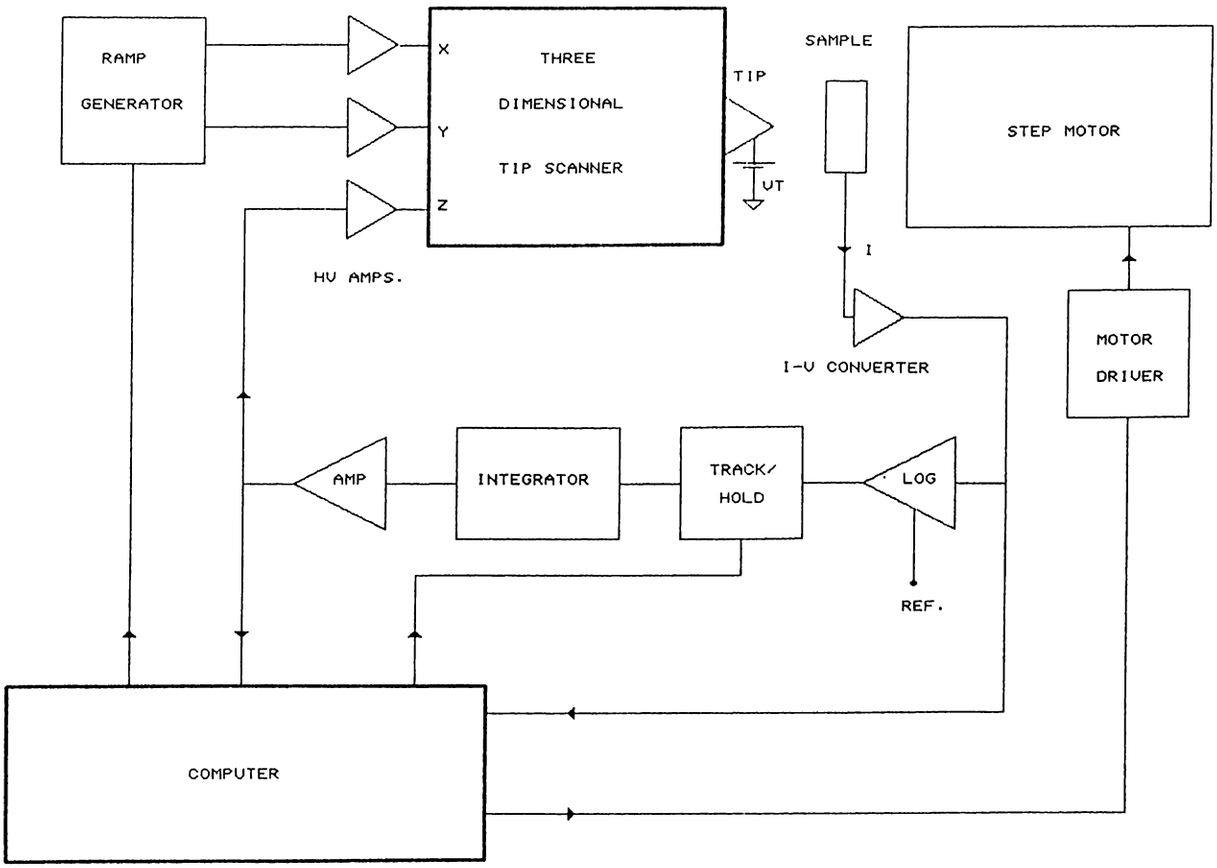

Figure 3.14. Block diagram of the STM electronics.

forth.

3.4.1 I–V Converter

The tunnel current is measured by using a low input current OP-AMP as shown in Figure 3.15. Positive input of the OP-AMP is grounded and the tunnel current is applied to the negative input. A large feedback resistor, R_f, is necessary to amplify very low tunneling currents. The output of the converter is then

$$v_o = R_f I_t \ . \tag{3.23}$$

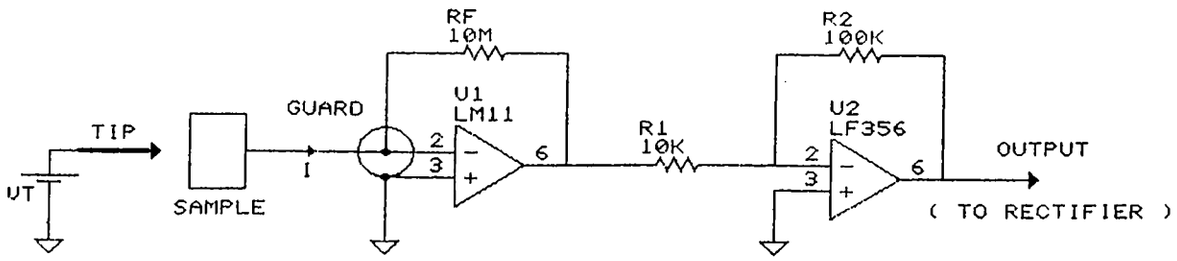

Figure 3.15. I–V converter.

LM11 bipolar, CA3420 and CA3140 BiMOS OP–AMPs were successfully used in our STM. Since the measured currents are very low, the printed circuit board must be carefully designed to eliminate the leakage and noise pickups. A guard ring which is connected to the ground, should be placed around the input pin to prevent the leakage currents. A coaxial cable should be used for connection from sample to the converter. The circuit and the whole STM must be shielded to reduce the hum. In addition, the current noise of the OP–AMP must be very low to reduce the noise level of the STM. $1/f$ noise is usually dominant for most of the amplifiers used. The gain of our converter is 100 mV/nA. The tunneling current is measured from a buffer amplifier, IC2.

3.4.2 z–Scanner Electronics

A home-made logarithmic amplifier is used to linearize the distance dependence of the tunnel current as shown in Figure 3.16. The input of the log amp must always be positive. Therefore, an active rectifier is used after the I–V converter. Output of the log amp is zero if the input current is 500μA. Therefore, equilibrium tunnel current can be adjusted by $R1$ and there is no need to use an additional comparator. Gain of the logarithmic amplifier is -1 *V/decade.*

Linearized and compared signal is integrated with IC6. Time constant,

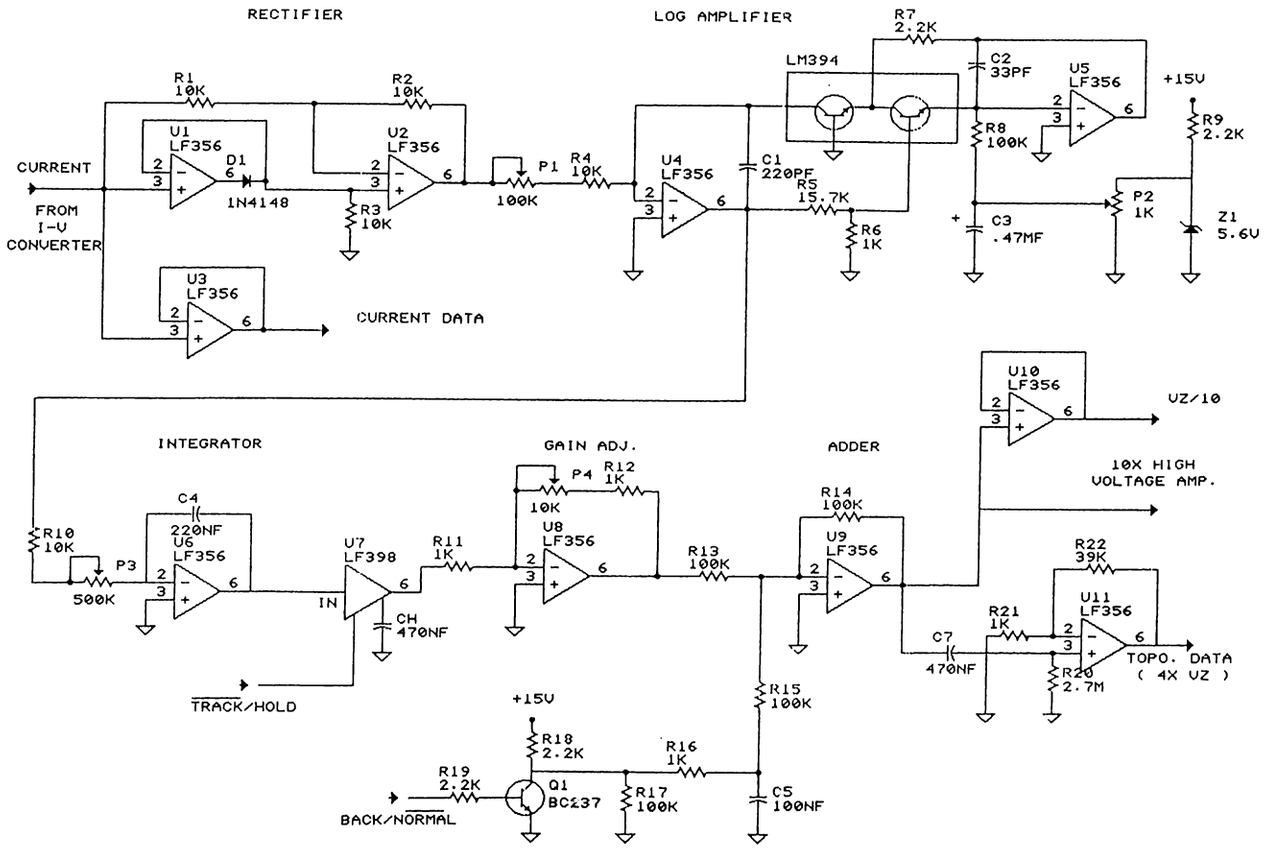

Figure 3.16. z–scanner electronics.

RC, of the integrator is adjusted by $P3$. LF398 Sample/Hold amplifier, which follows the integrator, is used to suspend the control temporarily. Then the signal is amplified with IC8 whose gain can be adjusted by $P4$.

Resulting signal drives the z–piezo through a $\times 10$ high voltage amplifier. A High Voltage amplifier was designed using an OpAmp and a few transistors. The circuit diagram of the amplifier is shown in Figure 3.17. Swings of up to 250 V_{pp} can be obtained if one uses ∓ 150V supply. The range of the scanner is approximately 6000 Å with this voltage swing. An *ac* coupled $\times 40$ amplifier, prior to the high voltage amplifier is used to record the piezo voltage. In addition, a buffer amplifier is used to record $V_z/10$ at the input of the high voltage amplifier.

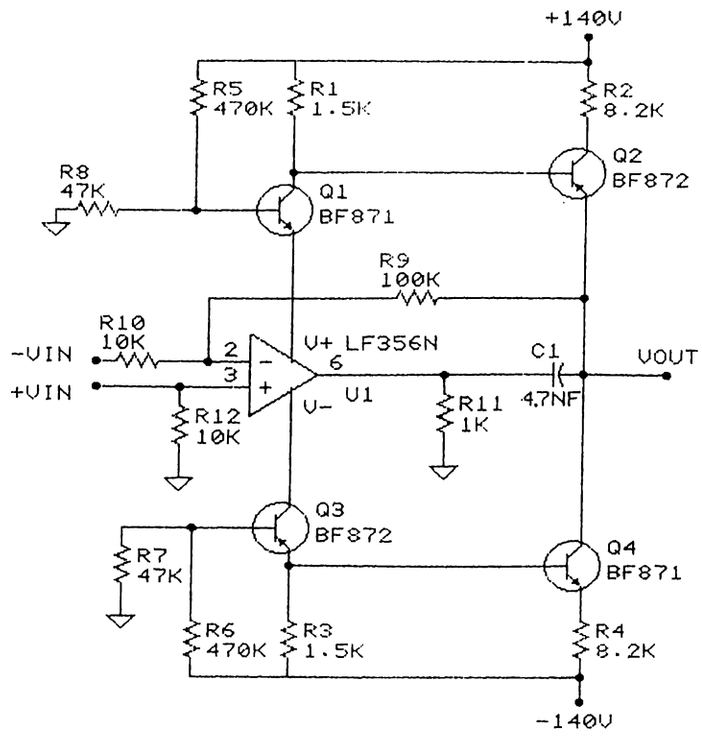

Figure 3.17. High Voltage Amplifier.

3.4.3 x&y Piezo Driver

Raster scan signals in x and y direction are generated by two 8-bit DACs as shown in Figure 3.18. The digital outputs of the data acquisition card are used to drive the converters. The image size is chosen to be 128 × 128 pixels. Therefore, LSBs of the DACs are grounded.

The scan area is set by changing the reference input to the DACs. Two high voltage amplifiers are used to apply scan signals to the piezos. The gain of the amplifiers can be changed between 1 and 10. $P2$ and $P3$ are used to position the tip to a specific part of the surface by applying offsets to the amplifiers.

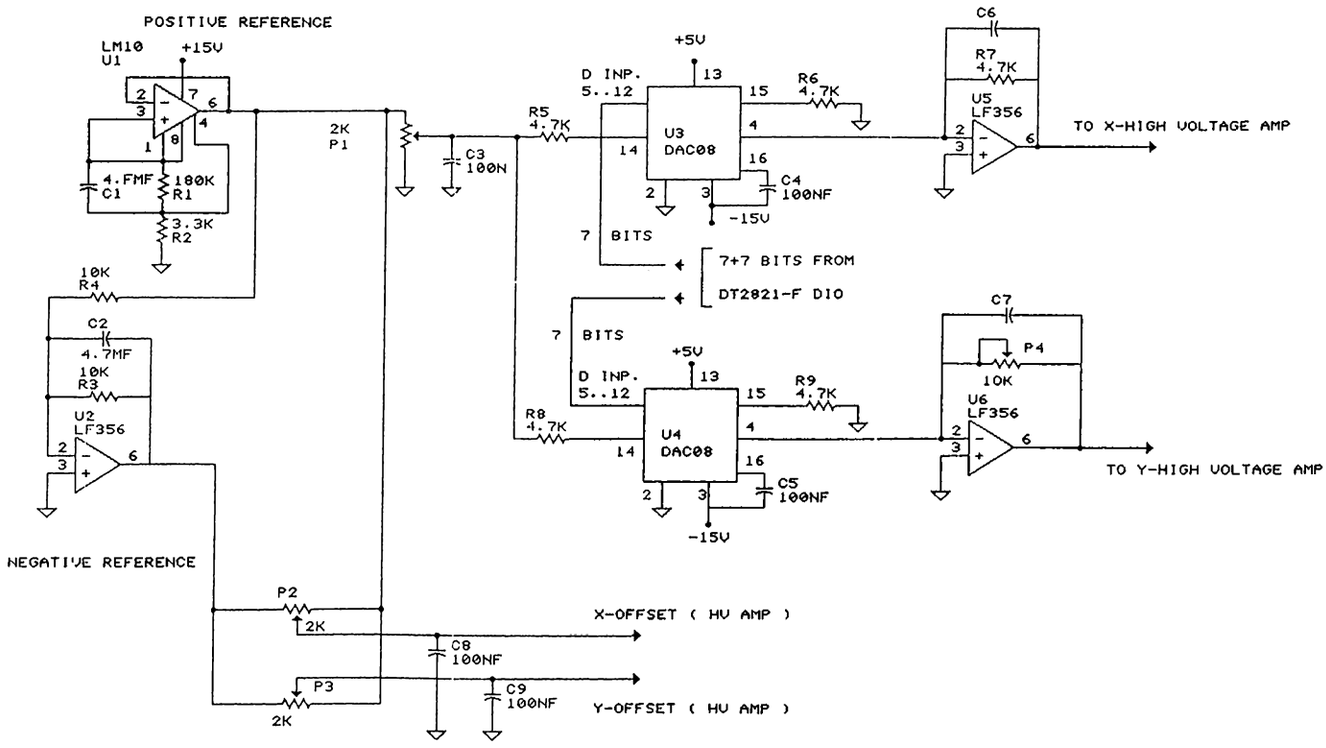

Figure 3.18. x–y Scanner Electronics.

3.4.4 Data Acquisition

The global control of the system is performed by a personal computer. The program approaches the sample towards the tip to start the tunneling. Once the tunneling has started, it keeps the sample in the dynamic range of the z–piezo. The code was written in Turbo PASCAL 4.0.

The data can be acquired in various ways. In constant current mode, the tip is slowly scanned over the surface and the tip position, v_z, is recorded. The scan speed and gain of the reading is selected by the user. At each point, four voltage measurements are averaged to eliminate the noise.

On the other hand, the tip is scanned over the surface very fast while the tunnel current is recorded in the constant height mode. It is fast enough not

to give any chance to the control loop to regulate the gap variations. Total image acquisition time is 0.4s in this mode. The gain of the A/D conversions can be specified by the user.

The data is stored in a 128×128 matrix. Top or 3–D view is displayed just after the data is obtained. It is possible to store the images in data files for further processing. Previous images can also be read from the mass storage to make comparison between surfaces.

3.4.5 Image Processing

Stored images are displayed and processed by another software. It is also written in Turbo PASCAL 4.0 and requires an EGA monitor on an IBM compatible PC/XT or AT. Procedures of the program can be selected from the menu. Images are read from the mass storage. Dynamic range of the image is calculated and divided into 16 levels. Each level is assigned to a different color. Image is plotted as a top view or a 3–D view with the associated false color to the each level. $\times 2$ zoom in top view is another choice. The color code is plotted just near the images to help to the user.

Tilt and rotation angles might be changed by the user to view the surface from different directions in 3–D display. The hidden lines are also eliminated for a clear display. In addition, images having a slope in any direction can be corrected by the program.

3.4.6 Low Pass Filter

Usually, recorded images have some noise. A digital Low Pass Filter (LPF) was implemented to eliminate some part of the noise. Standard digital LPF design techniques were not chosen, because we must take FFT (Fast Fourier Transform) and inverse FFT for each filtering operation. Instead, a convolution LPF is implemented for its simplicity and speed. A convolution window given

$W_{-1,-1}$	$W_{-1,0}$	$W_{-1,1}$
$W_{0,-1}$	$W_{0,0}$	$W_{0,1}$
$W_{1,-1}$	$W_{1,0}$	$W_{1,1}$

Figure 3.19. The convolution window.

in Figure 3.19 with coefficients ω_{ij} is scanned over the image. The pixel values of the image are updated as follows

$$z_{xy} = \frac{\sum_{ij} \omega_{ij} \times z_{x+i,y+j}}{\sum_{ij} |\omega_{ij}|} \qquad i,j : -1,0,1 \tag{3.24}$$

A filtered image can be seen in Figure 3.20.

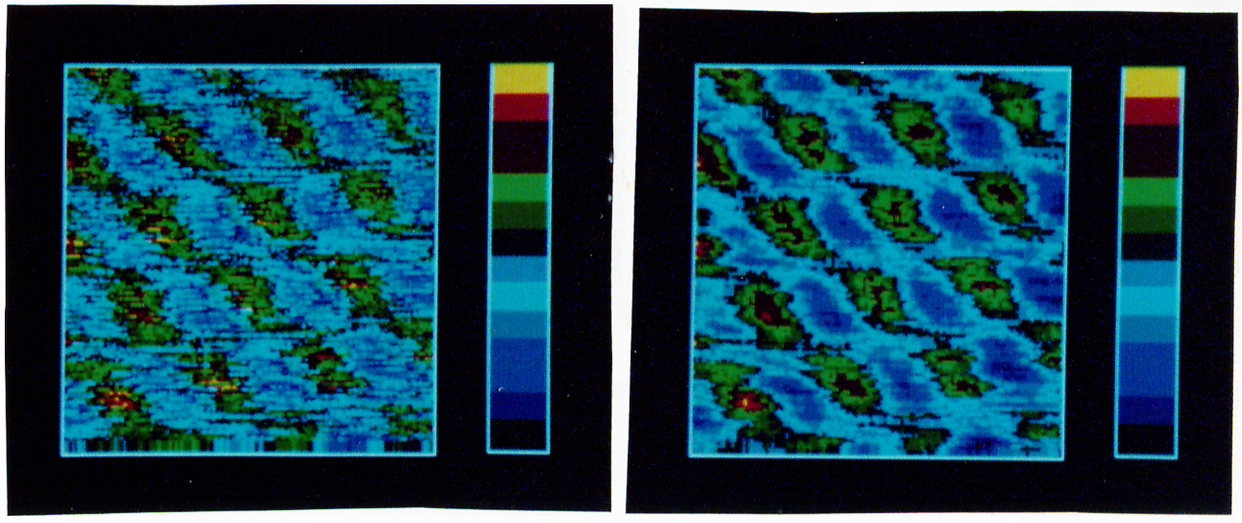

Figure 3.20. Low Pass Filter performance.

(a) Raw data (b) filtered image. The image size is approximately 9×11 $\AA^2$.

High Pass Filter can also be obtained easily, by changing the filter coefficients ω_{ij}. Moreover, Laplacian, Sobel or other types of kernels might be used for the edge detection.

3.4.7 Median Filter

The data may sometimes be corrupted with spiky noise called *Popcorn Noise*. A LPF can not remove this type of noise. A Median Filter works very well for this purpose. A 3×3 window is scanned over the data matrix. The pixels just below the window are sorted and the median of this sequence is assigned to the central pixel. The Median Filter can not be described mathematically like a LPF. Figure 3.21 shows an image processed with a Median Filter.

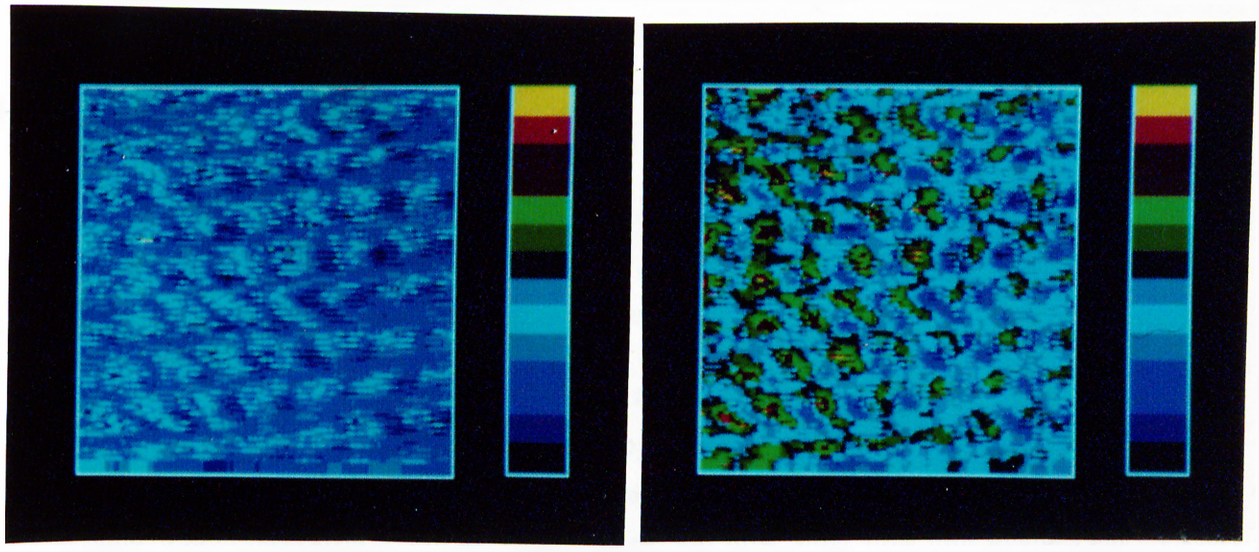

Figure 3.21. Median Filter Performance.

(a) Raw data (b) filtered image. The image size is approximately 14×18 $\mathring{A}^2$.

Chapter 4

Related Techniques and Applications

Invention of Scanning Tunneling Microscopy made a great impact on surface science. Beforehand, there was no tool to observe surfaces with the ultimate resolution. Various metal and semiconductors have been investigated first. Subsequently, biological samples, superconductors, adsorbed atoms on various surfaces etc. have been analyzed with STM.

Moreover, applications to the other fields started immediately. STM lithography, Scanning Tunneling Spectroscopy, Scanning Tunneling Potentiometry, electrochemistry are some of the examples.

Other types of interactions between a probe and a sample in contrast to tunneling , can also be used for microscopy. SXM stands for those microscopes, where X denotes the type of the interaction. Interactions such as Optical near fields, interatomic forces, capacitance, ion flow, heat flow and evanescent optical fields were successfully used in SXM with resolutions ranging from 1 to 1000 Å.

In this chapter, we will review applications of STM and related techniques, the SXM.

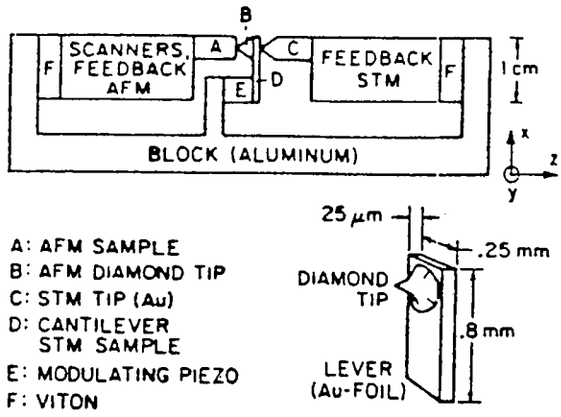

Figure 4.1. Atomic Force Microscope.

(After Ref. [45])

4.1 Atomic Force Microscopy

Atomic Force Microscope can image insulators, as well as metals and semiconductors in contrast to STM. Interatomic forces between a very sharp tip and sample is measured in Atomic Force Microscopy developed by Binnig *et al.* [45].

Figure 4.1 shows schematic diagram of the first Atomic Force Microscope (AFM). It is very common to measure forces by using springs. A small cantilever beam is used as a spring in AFM. Spring constant should be as small as possible to measure interatomic forces which are of the order of 10^{-9} N. In addition, the resonant frequency of the lever, $f_0 = \frac{1}{2\pi}\sqrt{k/m}$ must be high enough to isolate the microscope from external disturbances. This trade off between f_0 and k can be eliminated by reducing the dimensions of the lever. Gold foils [45], tiny tungsten and gold wires [46, 45] have been used to make AFM cantilevers. Very high performance springs with $\sim$ 30 KHz resonant frequency and 2 N/m spring constant have been microfabricated with conventional Silicon technology [47].

Miniature SiN cones can be evaporated or a small diamond piece can be

glued at the end of the microlever as a tip.

Displacement of the spring deflection is detected by a STM, tunneling to the lever. Back side of the cantilever beam is metal coated for tunnel detection of the spring movement. Most of the AFM uses tunneling for distance (force) measurement. Optical beam deflection [48] has also been used for this purpose. A laser beam is deflected from a mirror attached to the cantilever and reflected beam falls on a position sensitive detector placed at $\sim$ 10 cm away.

Moreover, capacitive and Interferometric position sensors [49, 46] with various configurations have successfully been operated as force sensors in Atomic Force Microscopes.

The microscope can operate in various modes. In the first one, the sample is vibrated at the resonant frequency and deflection in the spring detected with STM. In the second mode, the lever is vibrated at the resonant frequency. The resonant frequency changes, since the spring is loaded with the interaction force. Change in the amplitude or phase in tunneling current can be used to drive a feedback system. In the third mode, static deflection of the cantilever is measured to obtain the force directly, but due to thermal drift and other factors the spring constant, k drifts around its nominal value very much during the experiments. Hence, this mode is not very reliable.

Data is obtained in a very similar way to STM. Sample is scanned while keeping the force or the interelectrode separation constant.

Atomic resolution has been obtained on graphite, mica and various materials using AFM. Some images taken with AFM are displayed in Figure 4.2.

Martin and Wickramasinghe [50] modified AFM to investigate magnetic interactions. They used a magnetized tip in their Magnetic Force Microscope to map the magnetic domains in 1000 Å scale.

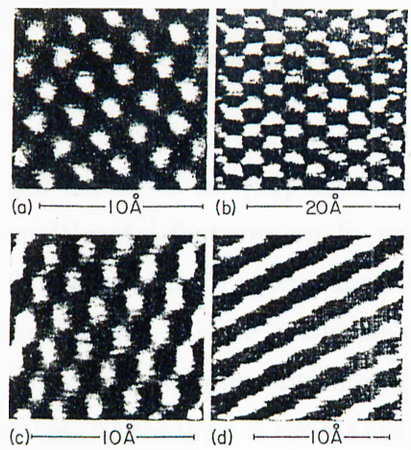

Figure 4.2. Some AFM images.

(a)Graphite (b) Molybdenum disulphide (c) Boron nitride (d) due to multiple tip atoms (after Ref. [47]).

4.2 STM Lithography

The lithography is the most important process in semiconductor device technology. Currently, photolithography is the commonly used technique, but it's resolution is diffraction limited to approximately $1\mu m$.

Device size must be reduced to increase the speed and decrease power consumption of integrated circuits. Device sizes are directly limited by the resolution of the lithography technique used. Electron beam and X-ray lithographies have been developed to reduce the linewidth of Integrated Circuits down to 10 nm.

STM lithography is very similar to e-beam lithography in principle. However, low energy electrons, $\sim$ 15 eV are used in contrast to KeV electrons used in e-beam lithography. Since tunneling electrons are confined in a very small area, the resolution is excellent. The first results giving $\sim$ 20 nm linewidth with Si are quite promising.

McCord and Pease [51] used calcium floride and aluminum floride as a photoresists and drew 20 nm lines with STM operating in field emission mode.

The photoresist is removed by tunneling electrons. They have also obtained 22 nm wide Gold-Palladium metal lines on Si substrate with PMMA resist using lift-off technique [52].

Ehcrics *et al.* [53] and Silver *et al.* [54] used organometallic gases such as DMCd, to deposit small metal features on Si substrate. For deposition, 10–15 V pulses with 10–100 ns duration are applied to the tip during the normal tunneling. 10nm features can be recorded on Si with this method. Residual atoms which exist in the vacuum chamber (mainly carbon) can also be deposited on Si substrates. These type of resists are called the contamination resist.

Similar results have been reported on gold substrates with 20 Å features [55]. However, these features disappear in a very short time due to high surface diffusion of gold.

Heinzelmann *et al.* [56] have formed 750 Å diameter holes on a $HoBa_2Cu_3O_{7-x}$ $Hi - T_c$ superconductor by pulsing the tip voltage.

Small molecules having 5 Å diameter, can be deposited or removed samples coated with organic materials [57]. But these results are not very reproducible.

Very recently, Albrecht *et al.* [58] have formed holes on graphite as small as 20 Å in diameter. The holes are formed by applying 3–5 V short pulses to the tip during tunneling. The method is highly reproducible that 99.6% of the intended holes were formed. They have carried out some controlled experiments to understand the physical process and found out that the water is essential for the hole formation. They proposed possible chemical reaction between carbon and water during the voltage pulses.

C.F. Quate and his students work on data storage by using Scanning Tunneling Microscope. The state of the art technology in mass storage now uses $\sim 10^9$ atoms to store one bit information [59]. The theoretical limit is calculated to be 100 atoms/bit. This figure corresponds to approximately 10×10 Å region on a crystal surface. Writing and reading features in that size

is possible with the STM, but the reproducibility is poor.

However, writing on and reading from $\sim 100 \times 100\mathring{A}^2$ cells seems feasible. If tracking the data and other technical problems could be solved, 10 GBits on a 1×1mm 'disk' is not a dream.

4.3 Near-field Optical Scanning Microscope

If a very small aperture compared to the wavelength, is used as an antenna, the diffraction limit can be beaten in optical microscopy. In 1972 Ash *et al.* [60] used very small apertures with 3 cm wavelength microwaves to image features as small as $\lambda/20$.

Near-Field Optical Scanning Microscope first introduced by Pohl [61] in 1984. They formed a very small aperture ($\sim$ 20 nm) at the apex of a very sharp metal coated quartz tip. The tip is brought very near to the sample. A laser beam is coupled to the tip and the sample is illuminated through the aperture. Since aperture to sample distance is of the order of aperture size, light is transmitted to the sample without any divergence. Thus, optical properties of surfaces can be investigated with very high spatial resolution, of the order of the aperture size. The aperture is scanned over the surface and transmitted light intensity is measured with a photomultiplier tube. Features as small as 20 nm have been observed [61].

The resolution of the microscope strongly depends on the aperture size and aperture–sample distance. Usually, tunneling between sample and metal coating of the antenna is used to keep interelectrode separation constant. Beside transmission, microscope can be operated in reflection [62] and collection [63] mode.

Very thin glass pipettes with apertures as small as 20 nm can also be used after coating sidewalls with metal film [63]. Recently, Fischer and Pohl [64] have observed single particle plasmons with NFOS.

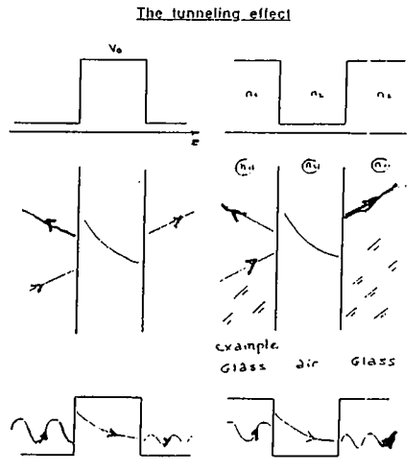

Figure 4.3. Photon 'Tunneling' through the barrier.

(After Ref. [66]).

4.4 Scanning Tunneling Optical Microscope

This is a fairly new technique for optical microscopy. Tunneling photons through the barrier rather than the electrons are used in the microscope [65, 66]. There is a strong analogy between electrons and photons. That is the wave equations describing them, have the same form.

Consider the glass–air interface as shown in Figure 4.3. If an incident beam is coming with an angle such that the beam is totally reflected from the interface, the electric field in 'barrier' (air) region is evanescent. That is the magnitude of the electric field drops exponentially with characteristic decay length, ξ (skin depth). This means that there is a non-zero probability to find a photon at that region. Hence, photons can 'tunnel' through the barrier, if another optical medium (in which photons can propagate) brought very close to the interface.

The sample illuminated from backside with a laser beam such that the evanescent field is formed on the surface. A chemically etched fiber tip is used to probe that field. Intensity of the field is measured with a photodetector. Resolution of the microscope is $\sim$ 20 nm in lateral and $\sim$ 3nm in z direction.

With a He-Ne laser (λ=633 nm), those figures correspond to $\lambda/30$ and $\lambda/200$ in lateral and normal directions, respectively. Scanning Tunneling Optical Microscope can be used to probe near fields in Integrated Optics.

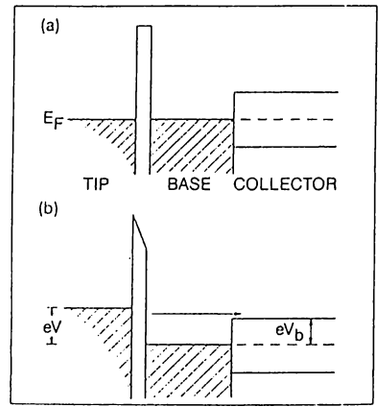

Figure 4.4. Energy levels in BEEM.

(After Ref. [67]).

4.5 Ballistic Electron Emission Microscope

Investigation of interfaces such as Schottky barriers, heterostructures etc. are very important in Solid State Physics. Although the conventional techniques (I–V, photoresponse etc.) work well for most of the cases, they all lack in the spatial resolution. Ballistic Electron Emission Microscope (BEEM) [67] which has been developed by Kaiser *et al.*, uses ballistic penetration of tunneling electrons into the interface region of a heterostructure. If a very thin, ~100Å, metal film is grown on a semiconductor sample tunneling electrons can reach to the interface balistically because the thickness of the metal is smaller than the mean free path of the electrons. The interface states can be probed with these electrons. Figure 4.4 shows the energy diagram of BEEM. If tip base bias is smaller than the junction barrier, V_b, energy of the tunneling electrons is not sufficient to jump the potential step at the interface and there will be no collector current. If tip bias is larger than the junction barrier, some of the

electrons can be transmitted to the collector, resulting in a collector current. Hence, Schottky barrier (SB) height can be measured directly. Furthermore, variation of the barrier with nanometer resolution can be mapped.

Kaiser *et al.* [67] measured SB height in Au-Si and Au-GaAs junctions with a 20 Å spatial resolution.

4.6 Scanning Tunneling Potentiometry

Tunnel current in STM can be written as

$$I = \frac{V}{R_t(V,d)} \tag{4.1}$$

where $R_t(V,d)$ is voltage and distance dependent tunnel resistance. Topography of the sample is obtained if the voltage and tunnel resistance are kept constant during constant current scan mode. If R_t and d is kept constant during the scan, voltage distribution over the surface can be resolved with very high resolution. This method, first introduced by Muralt and Pohl [68], is called Scanning Tunneling Potentiometry (STP).

The sample is biased with a dc source causing a surface potential $V(x,y)$. The tip is biased with an ac voltage. Resulting ac part of the tunnel current is rectified and used to keep the tunneling gap constant. Another bias voltage is added to the tip voltage to null the dc tunneling current by means of a feedback circuit. Therefore, this additional bias voltage added to the tip belongs to the surface potential at that particular point.

First results are obtained with 10–100 mV minimum resolvable voltage and a few angstrom lateral resolution on highly resistive metals. Potential distribution on a DH laser diode has been observed with $\sim$ 100 nm resolution [69]. Kirthley *et al.* [70] and Pelz and Koch [71] developed phase sensitive techniques to increase the voltage resolution to 1 μV.

4.7 Secondary Particle Emission in STM

Field evaporation methods are used to fabricate very sharp, monatomic tips [72]. Very interesting property of those tips are the capability of emitting collimated beams of electrons with a divergence of around 0.5 degree. The source is virtually a point source, because electrons are emitted from a single atom at the apex of the tip. A low voltage (10–15 V) Scanning Electron Microscope [72] has been successfully operated with this point electron source. Features as small as 30 Å have been resolved on polycrystalline gold sample.

Projection Electron Microscope [73] which also uses point electron sources, is an alternative to Transmission Electron Microscope. A rather divergent beam is directed on a very thin sample which is suspended on a hole at the anode. The source is very close to the sample. Transmitted electron fall on flourescence screen placed at 10–15 cm away from the source. The configuration is something like a slide projector. Since tip–sample separation is very small ($\sim$ 100 Å) very high magnifications can be obtained on the screen. Magnification can be adjusted by changing the position of the tip.

Allenspach and Bischof [74] detected spin polarized secondary electrons emitted from magnetic samples in STM operating in field emission mode.

Another interesting phenomena is the photon emission from samples during STM experiments. The physical mechanisms responsible for photon emission are scattering of hot electron with surface plasmons, inelastic tunneling through the barrier, direct radiation or thermalization. Spectroscopic data can be obtained by varying the tip voltage. Isochromat spectroscopy on Si reveals similar patterns to inverse photoemission spectra [75]. Photon map of the samples can be plotted with approximately 3 Å resolution in addition to the topography.

4.8 Scanning Tunneling Spectroscopy

Since tunneling current also depends on the surface density of states at the Fermi Level, surface states can also be directly probed with the Scanning Tunneling Microscope. Advantage of the Scanning Tunneling Spectroscopy (STS) with respect to conventional surface techniques is its ability to perform spatially resolved spectroscopy on surfaces.

Superconductors have been analyzed with this technique. Superconductive energy gap, Δ, have been observed in conventional [25] and Hi-T_c [76] superconducting materials. The gap changes in 1 μm range in $YBaCuO$ single crystal samples have been observed with spatially resolved spectroscopy.

For finite bias voltages tunneling current is given by

$$I_t = \int_0^{eV} \rho_s(E)\rho_t(E - eV)T(E, V) \tag{4.2}$$

where, ρ_s, ρ_t, E and $T(E, V)$ are surface and tip densities of state, energy with respect to Fermi level and transmission coefficient between tip and surface states. The transmission probability can be calculated by WKB approximation as [77],

$$T = exp\left\{-2s\left[\frac{2m}{\hbar}(\phi - E - \frac{eV}{2})^{1/2}\right]\right\} \tag{4.3}$$

where ϕ is the average barrier height for the sample and the tip.

Interpretation of this expression is as follows; states having lower energy than Fermi level at the tip also contributes to the tunneling in finite bias condition. However, low lying states are faced with larger barrier than the Fermi level states as shown in Figure 4.5. Therefore states with larger E contributes most strongly to the tunneling. Transmission probability drops by one order of magnitude for 1 eV reduction in energy, E. Hence, tunneling

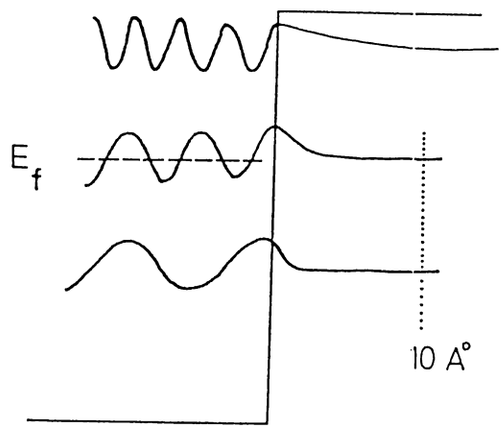

Figure 4.5. Form of the wavefunctions for various energies.

Transmission probability drops for low lying states due to increased barrier widths for those states (After Ref. [77]).

current can be approximated to

$$\begin{aligned} I &\simeq \rho_s(eV)exp(-2\kappa s) \qquad for \qquad V > 0 \\ I &\simeq \rho_s(E=0)exp(-2\kappa s) \qquad for \qquad V < 0 \end{aligned} \tag{4.4}$$

where $\kappa = \sqrt{\frac{2m}{\hbar}(\phi - \frac{eV}{2})}$.

In constant current spectroscopy, tip voltage is changed while measuring the conductivity. But, the voltage can not pass through zero, otherwise the tip would touch to the sample. In constant distance mode, however, the feedback loop is temporarily disabled by a Sample/Hold circuit, then the voltage is varied and the differential conductivity is measured. Normalized conductivity, $(dI/dV)/(I/V)$, rather than the conductivity itself, is analyzed to remove low voltage divergence of the conductivity. Spectra obtained on Si and GaAs [77] samples reveal density of states of semiconductors, displaying the power of the method.

4.9 Detection of Gravity Waves using STM

Gravity waves are emitted from Astrophysical sources, such as Supernova explosions. Since 1950's, the detection of gravity waves are the subject of very challenging research. Calculations have shown that measurement of length changes of the order of $\frac{\delta l}{l} = 10^{-21}$ was necessary to sense the gravity waves. There are two approaches for Gravity Wave Antennas (GWA): Michelson interferometer type detectors with huge dimensions (4-5 Km) and massive antenna, known as Weber bars [78].

Mechanical displacements at the end of a Weber bar is estimated [79] to be approximately 10^{-11}Å for typical GW amplitudes. This figure is very small to be detected with the available sensors. Therefore, mechanical transformers play very important role to amplify these extremely weak signals. If a second oscillator having a much smaller mass $m_2 = \mu m_1$ and same resonant frequency, coupled to the oscillator (the Weber bar), some part of the energy is transferred to the small oscillator. The gain of the transformer is $\sqrt{1/\mu}$. If one couples n oscillators with decreasing mass the transformer becomes broadband and the gain is again given by end to end mass ratio $\sqrt{m_2/m_n}$. This type of transformers have been analyzed by Blair *et al.* [80].

A broadband antenna is essential for gravity wave detection, because the frequency of the waves coming from the space is not well-known. A better transformer can be built by continuously changing the acoustic impedance of the transformer, like an ear trumpet. In principle, the transformer can be coupled to any kind of transducer, piezoelectric, capacitive, inductive or interferometric. Very small relative displacements, as small as 10^{-4} Å can be detected a by tunneling transducer. Although distance sensitivity of the tunnel probe is relatively poor compared to the other methods, its capability to operate on very small dimensions, down to atomic scales, the overall performance have been estimated to be far superior.

Another interesting property of the tunnel probe is being a reduced back-action, non-reciprocal transducer [81]. The back-action of the transducer is

only due to the momentum transfer of tunneling electrons transmitted to the transformer and to the capacitive coupling resulting from small capacitance of tunnel junction.

With a $10^6 - 10^7$ gain transformer implemented by a microfabricated SiO_2 lever and a tunneling probe with 10^{-4}Å sensitivity, Gravity waves would seem to be observed [79, 82]!

4.10 Scanning Capacitance Microscope

Near-Field Scanning Capacitance Microscope has been demonstrated by Matey and Blanc [83] with 0.1 μm resolution. Williams *et al.* [84] have improved the technique and reached 25 nm resolution. They have used RCA Video Disc capacitive sensor to measure the capacitance changes as low as 10^{-19}F in 1 KHz bandwidth. Scanning Capacitance Microscopy could be useful to probe dielectric properties of the surfaces in nm scale. They have found that theoretical limit for resolution is $\sim$ 10 nm, if capacitance changes of 10^{-22} F can be detected.

4.11 Scanning Ion Conductance Microscope

Scanning Ion Conductance Microscope [85] has been developed to image insulated samples covered with electrolyte, especially biological samples. An electrolyte filled micropipette is used as a 'tip'. Since surface is immersed in a different type of electrolyte, there exists an ion flow between electrolytes through the pipette hole. If pipette approaches to the sample, ion current changes. Therefore topography of the image can be obtained by recording the current variations or pipette's height variations while scanning the pipette over the surface. A membrane filter has been imaged with a 0.5 μm ID pipette and 0.8 μm holes on the membrane have been resolved [85]

4.12 Application of STM to Biology and Chemistry

Biological systems have been an attractive field for STM since the invention of the microscope. Most of the biological samples lack in conductivity and therefore, they should be covered with metalic films before imaging with STM. The resolution is limited by the grain size of the film, which is ~ 2 nm. Amrein *et al.* [86] have observed recombinant–DNA complexes coated with Pt/Ir/C film, using STM. They have resolved the helix structure of DNA. Bacteriophage T4 virus has also been studied with STM.

Very recently, naked DNA adsorbed on gold substrate has been imaged by Cricenti *et al.* [87]. They have resolved the helicity and pitch period of DNA.

Monolayer films of organic materials have great importance in lithography, surface chemistry and biology. For example, PMMA (poly methyl methacrylate) and some special polymers are used as a resist in e-beam lithography.

Direct imaging of these systems gives information about the microstructure of the molecules. The structure of these systems can not be observed with conventional electron microscopy techniques, because high energy electrons damage the sample.

Graphite is a very good substrate for chemical and biological adsorbates. Atomically flat very large terraces can be easily obtained by cleaving with a Scotch tape.

Dovek *et al.* [88] have investigated PMMA, PODA (poly octadecyl-acrylate) and PMTS (poly 2-methyl-1-pentene sulphone) films on graphite substrates. They have also modified the adsorbed polymers by applying short voltage pulses to the tip. Smith *et al.* [89] have observed lipid bilayers adsorbed on graphite with Scanning Tunneling Microscope.

Liquid crystals are another interesting systems studied with Scanning Tunneling Microscope. 8CB (cyanobiphenyl) [90] as well as 10CB and 12CB [91] liquid crystals on graphite surface have been observed by different

groups.

Foster *et al.* [57] have imaged *diphtalate* molecules by pinning them onto the graphite surface. They have covered the graphite by a drop of *diphtalate.* Application of $\sim$ 3V pulse to the tip pins the molecule during the normal operation of the microscope. Very surprisingly, the process is reversible. Application of another pulse removes the molecule with resulting a clean substrate behind it. Sometimes, 'erasing' is performed partially and a benzene ring is left at the surface. They explained this as cleaving the molecule, because benzene ring is one of the constituents of the *diphtalate.* Ohtani *et al.* [92] have observed the benzene coadsorbed with carbon monoxide on Rh (111) surface using STM.

STM can also operate in liquids. Atomic resolution in various liquids (such as oils , water, sea water) on graphite substrates have been reported. Therefore, STM can be an interesting tool for potential electro chemical applications. Topographic and spectroscopic studies of metal-electrolyte interactions and very high resolution electrolithography are some of them.

STM for electro chemical applications should be designed carefully. The tip, (except the apex) should be insulated, to overcome Faradaic currents in aques environment. The STM, is very promising tool for electrochemistry, because, the surfaces of the electrodes can be imaged with atomic resolution during the electro chemical processes, which was not possible before. Trevor *et al.* [93] have observed the *in situ* roughening, annealing and dissolution of Gold(111) surface in an electrochemical cell. Lin *et al.* [94] have reported photo electrochemical etching of a depth of 0.3 μm in n-GaAs using STM in an electrolyte.

Chapter 5

Results

We have investigated Highly Oriented Pyrolithic Graphite (HOPG) samples with our Scanning Tunneling Microscope. Graphite is the most suitable material for STM studies. Because, it has layered structure and large, atomically flat areas can be obtained easily by peeling of the top layers of the crystal. It is an extremely inert material so that, atomic resolution in various environments such as UHV, air and liquids have been reported in the literature. It can also be used as a substrate for biological and chemical species.

Carbon is a tetravalent atom, having one $2s$ and three $2p$ valence electrons. sp^2 hybridization of the orbitals leads to the hexagonal structure of the graphite. The remaining $2p$ orbitals weakly interact with the other layers and hold them within the crystal.

The structure of the graphite crystal can be seen in Figure 5.1. Each monolayer is shifted with respect to each other in the lateral direction. Half of the atoms in the monolayer has neighboring atoms in the neighboring layers. These atoms are labeled as A-type atoms. The other type of atoms have center of hexagons directly below or above them and designated as B-type atoms. Furthermore the center of the hexagon is called H-site.

The primitive translation vectors of the lattice are as follows

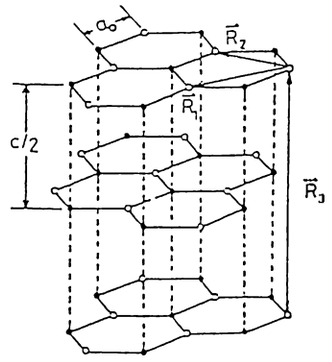

Figure 5.1. Structure of the graphite.

(After Ref. [17])

$$\begin{aligned} \vec{R}_1 &= (\ \sqrt{3}a_0, \quad 0, \quad 0) \\ \vec{R}_2 &= (\frac{\sqrt{3}}{2}a_0, \ \frac{3}{2}a_0, \quad 0) \\ \vec{R}_3 &= (\quad 0, \quad 0, \quad c) \end{aligned} \tag{5.1}$$

where $a_0 = 1.418$ Å is the nearest neighbor distance and $\frac{c}{2}$=3.348 is the interlayer spacing [17].

Energy bands of the graphite have been calculated by several authors [96, 17]. For the monolayer, A and B sites are equivalent and the Fermi surface is squeezed into K point of the Brillouin Zone. Moreover, densities of state at the Fermi level is zero. Brillouin Zone of the graphite crystal is shown in Figure 5.2.

The bulk properties of graphite is very similar to that of monolayer. Interaction between $2p_z$ orbitals extends the point-like Fermi surface of the monolayer. The resultant Fermi surface of the bulk graphite has a cigar-like shape along K-P direction of the Brillioun zone [17].

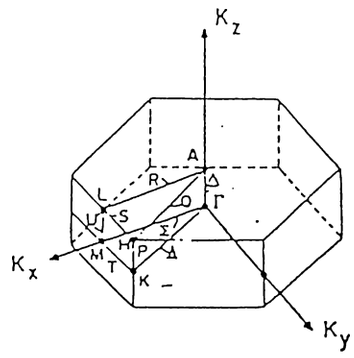

Figure 5.2. Brillouin Zone of the graphite.

(After Ref. [17])

According to the Tersoff–Hamann theory, STM images the charge density corrugation at the Fermi level. Therefore, we must be careful to interpret the STM images.

Selloni *et al.* [97] have calculated band structure of the graphite sample. They have found the charge corrugation at the Fermi level with amplitudes lying between 0.7–1.0 Å. They have also found a 0.05 Å corrugation difference between A and B type atoms.

Batra and co-workers [95] have calculated the band structure of graphite by self consistent field method. They have observed up to 1.5 Åcorrugation amplitudes for B and H sites. Moreover, they have pointed out ~0.5 Å corrugation between A and B type atoms. They explained the loss of trigonal symmetry in some STM images with slipped top-layer of graphite. However, this artifact can also be due to multiple tip effect. As we pointed out earlier, the tip is the most crucial part of the instrument. Mizes *et al.* [98] have investigated how tip structures change the STM images. If one has a two atom tip, the tunneling current is proportional to the sum of the local densities of state at the positions of the tip atoms. This approximation is based on random phase difference between the two tip atoms. They have shown that wide variety of images can be obtained by changing the relative phase of the tip atoms.

The multiple tip effect has also been observed on 7×7 reconstructed Si(111) surface [99] as doubling of atoms in the unit cell.

5.1 Experiments

We have used Highly Oriented Pyrolithic Graphite (HOPG) samples for our STM studies. The samples are cleaved by a Scotch tape stuck to the surface. The tips were freshly etched just before the experiment as is explained in the third chapter. The bias voltage was applied to the tip and the tunneling current is measured from the sample. The sample is bonded from its backside to an Aluminum sample holder with a conductive epoxy.

The microscope can be operated in constant current and constant height mode. The constant height mode images have lesser noise than images obtained by constant current mode, since fast scanning shifts the data to higher frequencies. Hence, the noise and data are separated in the frequency domain.

A graphite image obtained in constant current mode is shown in Figure 5.3. The voltage across the tunnel gap was 13 mV and tunneling current was 15 nA. The corrugation amplitude is approximately 1 Å. The image is consisted of 128×128 pixels. The tip was scanned with a speed of 40 lines/s and the image size is approximately 12×13 $\mathring{A}^2$.

Figure 5.3(a) is the three dimensional plot of the image. In Figure 5.3(b) the top view of the same data is presented. Positions of the inequivalent carbon atoms are marked on the top view. The full and empty circles belong to B-type and A-type atoms, respectively.

Since the local density of states is lower for an A-type atom than that of B-type atom [95], the former has a smaller corrugation.

Figure 5.4 shows a constant height image of a region on graphite sample with an area of 15×17 $\mathring{A}^2$. The tip bias was 50 mV and tunneling current was 1 nA for this particular run. The tip was scanned very fast and current

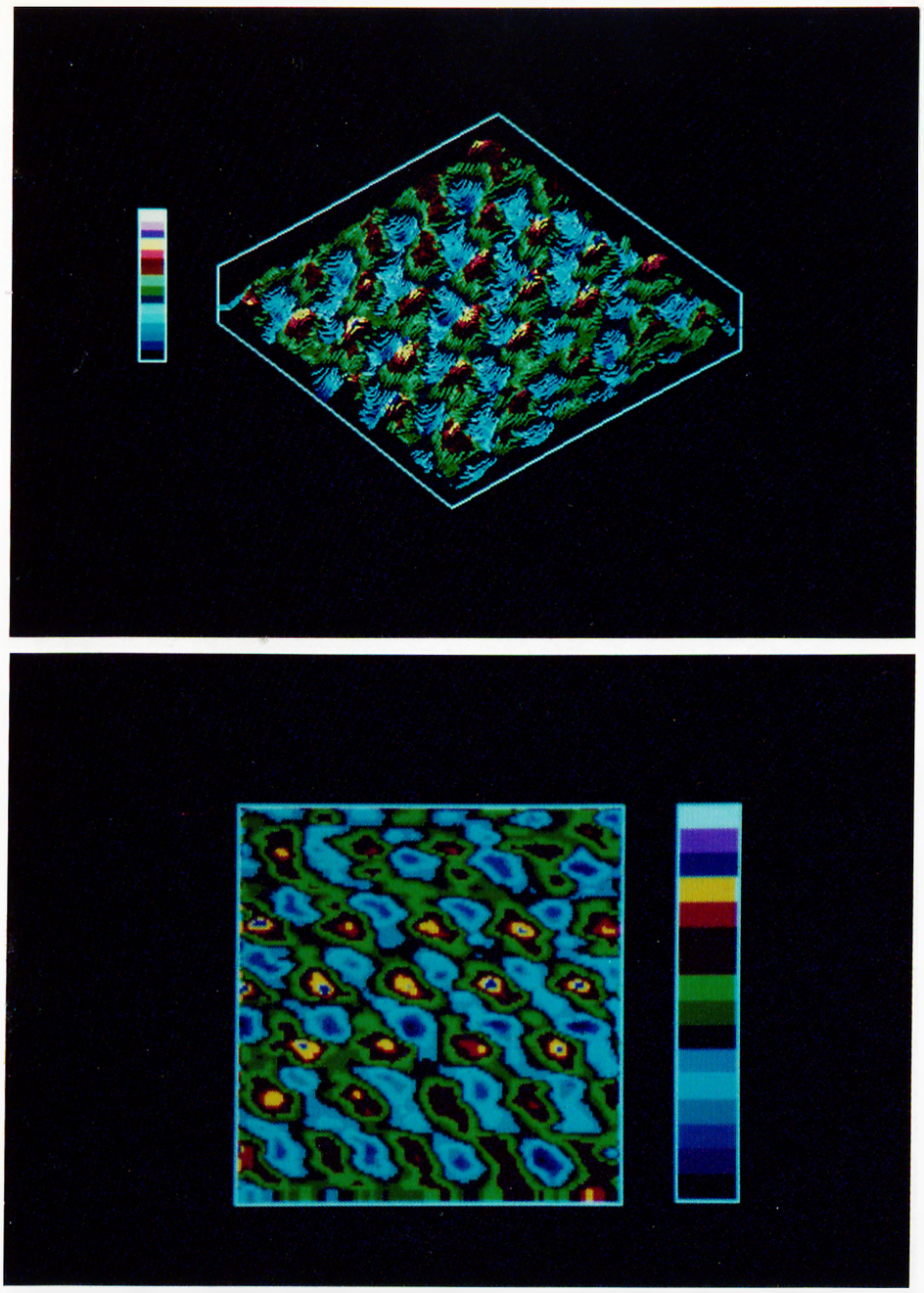

Figure 5.3. A constant current image of a graphite sample.

(a) Three dimensional plot (b) top view. The false color code is also given with the image.

variations were recorded. The data was acquired in 0.4 seconds. The peak-to-peak current corrugation is 0.25 nA. Note that the trigonal symmetry is clearly visible.

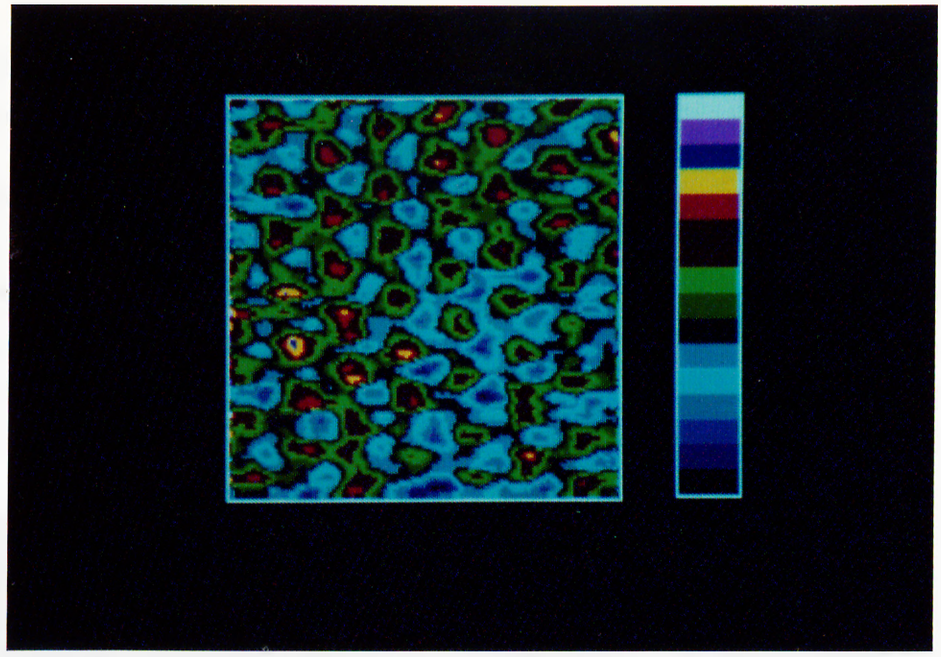

Figure 5.4. Constant height image of a graphite surface.

Image size is $\sim 15 \times 17$ $\mathring{A}^2$.

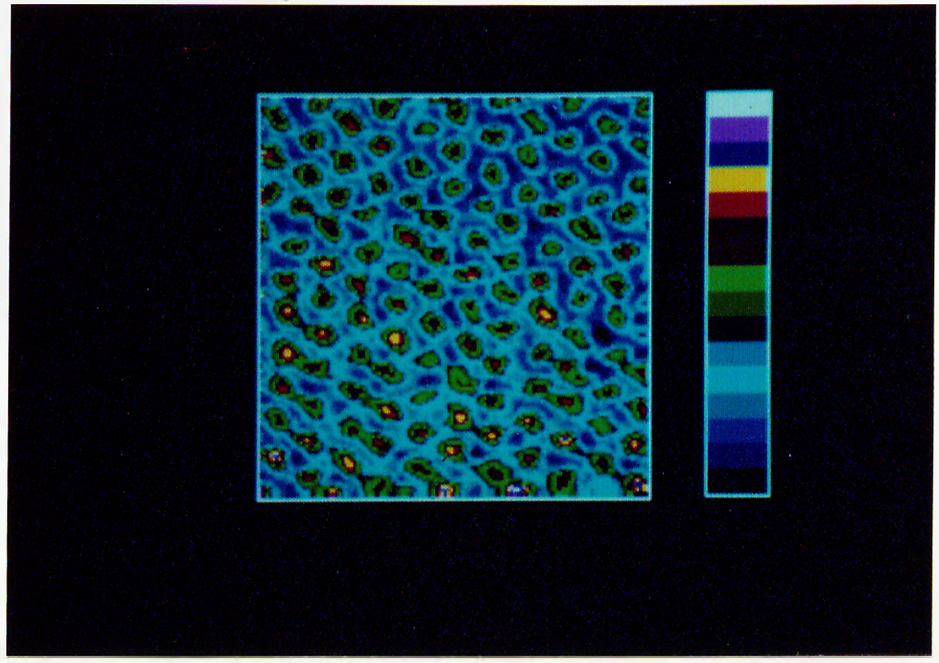

Figure 5.5. Another constant height image of a graphite surface.

Image size is $\sim 21 \times 27$ $\mathring{A}^2$.

Another constant height image of approximately 21×27 $\mathring{A}^2$ region on a

graphite surface is given in Figure 5.5. The tip voltage is 50 mV and resulting tunnel current is 2 nA. Peak-to-peak corrugation amplitude is 0.7 nA.

We have also found some anamoulus results in graphite. One can see the loss of trigonal symmetry in Figure 5.6. The hollow sites are displaced from the hexagonal center toward the center of the rhombus formed by the B-type atoms. This anomaly can be due to slipped top-layer proposed by Batra *et al.* [95]. Slipped top-layer can be easily formed while cleaving the sample, because the energy difference between the two configurations is very small.

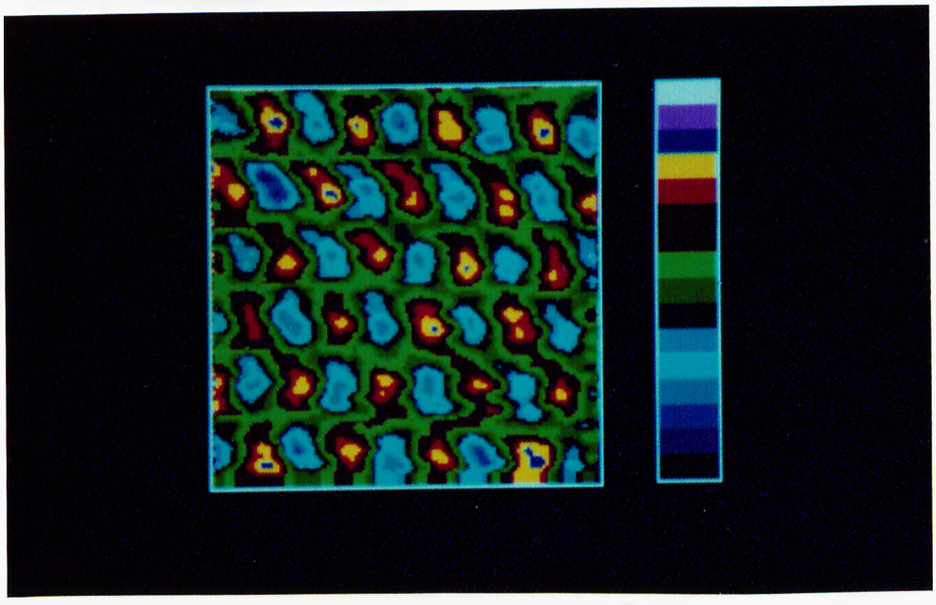

Figure 5.6. An anomalous image.

Loss of trigonal symmetry on the graphite surface is clearly visible. 11×13 $\AA^2$ region of a graphite surface. Tip voltage and tunnel current was 13 mV and 1 nA respectively. Peak-to-peak current corrugation is 0.46 nA.

Another possibility is again the multiple-tip effect. If we have more than one atom at the apex of the tip, we can image the unit cell of the graphite with different decoration inside it. Therefore, a strict conclusion is not possible if we do not know the electronic structure of the tip, which is the case, in most of the STM experiments.

We have calibrated our scanner by using graphite images obtained with

our STM. The lattice constant of the graphite, a_0=1.418 Å is well-known from X-ray diffraction measurements. We have found that the sensitivities of the scanner were magnified due to finite tip length. Because of leverage action of the x-y-z piezos, the sensitivities should be multiplied by $(1 + l_t/l_z)$, where l_t and l_z are tip and z-piezo lengths, respectively. Measured sensitivities are consistent with the calculated values.

Thermal drift of our STM was also measured using the obtained images. The thermal drift of our STM was found to be approximately 0.4 Å/min by comparing the successive scans.

Chapter 6

Conclusions

Scanning Tunneling Microscope made a great impact in surface science. It is the unique technique which images the surface electronic structures directly. Its atomic scale resolution opens fascinating fields in science and technology.

In this study, we have constructed a Scanning Tunneling Microscope which operates in air. The critical parts of the microscope are the vibration isolation and the sample approach systems. Stacked brass plates separated by rubber pieces and a heavy marble block sitting on bicycle tires are used for the vibration isolation. We also used small sand pools under the legs of the table on which STM is placed.

We constructed three models of STM. In the first one, a micrometer screw with lever reduction mechanism moves the sample towards the tip. We have observed the first tunneling with this configuration, but vibrational coupling during the sample approach was very large. In the second one, we constructed an electrostatic louse. Although we obtained tunneling, the louse did not work reliably and we could not operate the STM reproducibly.

We finally developed a step motor sample approach mechanism for the microscope. This new microscope operates very well in constant current mode, as well as in the constant height mode. Atomic resolution images of graphite (HOPG) surface has been obtained in both modes of operation. The

inequivalent atomic sites in the unit cell were also observed on the graphite surfaces. The performance of our STM (in terms of stability, thermal drift, scan ranges, results etc.) is similar to the microscopes described in the literature.

Furthermore, we have observed loss of trigonal symmetry in some of the images. These images are most probably due to multiple atoms at the apex of the tip, although the slipped top layer argument could also be considered as being responsible for this artifact. Hence, one must be careful to interpret the STM data.

Future plans include optimizing our instrument, investigating various materials and some novel applications. A Scanning Tunneling Microscope to be operated in Ultra High Vacuum conditions is planned for 'clean' experiments, in order to better understand the Physics of surfaces.

Bibliography

[1] J. R. Oppenheimer. *Three Notes on the Quantum Theory of Aperiodic Effects.* **Physical Review B.** 31:66,1928.

[2] R. H. Fowler and L. Nordheim. *Electron Emission in Intense Electric Fields.* **Proc. Roy. Soc. Lond. A** 119:173,1928.

[3] L.Esaki. *New Phenomenon in Narrow Germanium p-n Junctions.* **Physical Review,** 109:603,1958.

[4] I. Giaver. *Energy Gap in Superconductors Measured by Electron Tunneling.* **Physical Review Letters,** 5:157,1960.

[5] B. D. Josephson . *Possible New Effects in Superconductive Tunneling.* **Physics Letters,** 1:251,1962.

[6] P. Hansma. *Tunneling Spectroscopy. Ed.* **Plenum Press,** New York, 1982.

[7] R. Young, J. Ward and F. Scire . *The Topogrofiner: An Instrument for Measuring Surface Microtopography.* **Review of Scientific Instruments,** 43:999,1972.

[8] G. Binnig, H. Rohrer, Ch. Gerber and E. Weibel. *Tunneling Through a Controllable Vacuum Gap.* **Applied Physics Letters,** 40:178,1982.

[9] G. Binnig and H. Rohrer. *Scanning Tunneling Microscopy.* **Helvetica Physica Acta.** 55:726,1982.

[10] E. C. Teague. *Room Temperature Gold-Vacuum-Gold Tunneling Experiments.* **Bull. Amer. Phys. Soc.** 23:290,1978.

[11] U. Poppe. *Tunneling Experiments on a Single Crystal of* ERh_4B_4. **Physica B & C,** 108:805,1981.

[12] J. G. Simmons. *Generalized Formula for the Electric Tunnel Effect Between Similar Electrodes Separated by a Thin Insulating Film.* **Journal of Applied Physics,** 34:1973,1963.

[13] J. Bardeen. *Tunneling from Many Particle Point of View* . **Physical Review Letters,** 6:57,1961.

[14] J. Tersoff and D. R. Hamann. *Theory and Application for the Scanning Tunneling Microscope.* **Physical Review Letters,** 50:1998,1983.

[15] N. Garcia, C. Ocal and F. Flores. *Scanning Tunneling Microscopy: Application to Au(110) (1×2).* **Physical Review Letters,** 50:2002,1983.

[16] E. Stoll, A. Baratoff, A. Selloni and P. Carnevali. *Current Distribution in Scanning Tunneling Microscope: A Free-Electron Model* . **J Phys C,** 17:3070,1984.

[17] A. E. Tekman *Atomic Theory of the Scanning Tunneling Microscopy.* M. S. Thesis. Bilkent University, 1987.

[18] S. Ciraci, A. Baratoff and I. P. Batra, *Tip-Sample Interaction Effects in Scanning Tunneling and Atomic Force Microscopy.* to be published in **Physical Review B.**

[19] Sang-Il Park and C. F. Quate. *Theories of the Feedback and Vibration Isolation Systems for the Scanning Tunneling Microscope.* **Review of Scientific Instruments,** 58:2004,1987.

[20] Y. Kuk and P. J. Silverman. *Scanning Tunneling Microscopy.* **Applied Physics Letters,** 48:1597,1986.

[21] Ch. Gerber, G. Binnig, H. Fuchs, O. Marti and H. Rohrer. *Pocket-Size Scanning Tunneling Microscope (STM) Combined with a Scanning Electron Microscope (SEM).* **Review of Scientific Instruments,** 57:221,1986.

[22] J. W. Lyding, S. Skala, J. S. Hubacek, R. Brockenbrough and G. Gammie. *Variable-Temperature Scanning Tunneling Microscope.* **Review of Scientific Instruments,** 59:1897,1988.

[23] K. Takata, S. Hosoki, S. Hosaka and T. Tajima. *Scanning Tunneling Microscope with Reliable Coarse Positioners.* **Review of Scientific Instruments,** 60:789,1989.

[24] Douglas P. E. Smith and S. A. Elrod. *Magnetically Driven Micropositoners.* **Review of Scientific Instruments,** 56:1970,1985.

[25] A. P. Fein, J. R. Kirthley and R. M. Feenstra. *Scanning Tunneling Microscope for Low Temparature, High Magnetic Field and Spatially Resolved Spectroscopy .* **Review of Scientific Instruments,** 58:1806,1987.

[26] Sang-il Park and C. F. Quate. *Scanning Tunneling Microscope.* **Review of Scientific Instruments,** 58:2010,1987.

[27] G. W. Stupian and M. S. Leung. *A Scanning Tunneling Microscope Based on a Motorized Micrometer.* **Review of Scientific Instruments,** 60:181,1989.

[28] D. W. Pohl. **Review of Scientific Instruments,** 58:54,1987. Ph. Niedermann, R. Emch and P. Descouts. *Simple Piezoelectric Translation Devices.* **Review of Scientific Instruments,** 59:368,1988.

[29] Data Translation, Inc. 100 Locke Drive, Marlboro, MA 01752-1192, USA.

[30] Ismet Kaya. M. S. Thesis. Department of Physics, Middle East Technical University, 1990.

[31] B. L. Blackford, D. C. Dahn and M. H. Jericho. *High-Stability Bimorph Scanning Tunneling Microscope.* **Review of Scientific Instruments,** 58:1343,1987.

[32] G. F. A. van de Walle, J. W. Gerritsen, H. van Kempen and R. Wyder. *High Stability Scanning Tunneling Microscope.* **Review of Scientific Instruments,** 56:1573,1985.

[33] S. Akamine, T. R. Albrecht, M. J. Zdeblick and C. F. Quate *Microfabricated Scanning Tunneling Microscope.* **IEEE Electron Device Letters,** 10:490,1989.

[34] EBL Company, East Hartford, CT.

[35] G. Binnig and D. P. E. Smith. *Single-Tube Three-Dimensional Scanner for Scanning Tunneling Microscope.* **Review of Scientific Instruments,** 57:1688,1986.

[36] S. Çıracı, in *Basic Concepts and Applications of Scanning Tunneling Microscopy and Related techniques,* eds R. J. Behm, N. García and H. Rohrer (Elseiver, Amsterdam, 1990).

[37] Sang-il Park, J. Nogami and C. F. Quate. *Effect of Tip Morphology on Images Obtained by Scanning Tunneling microscopy.* **Physical Review B.** 36:2863,1987.

[38] Y. Kuk and P. J. Silverman. *Role of Tip Structure in Scanning Tunneling Microscopy.* **Applied Physics Letters,** 48:1597,1986.

[39] R. J. Colton, S. M. Baker, J. D. Baldeschwieler and W. J. Kaiser. *"Oxide-free" Tip for Scanning Tunneling Microscope.* **Applied Physics Letters,** 51:305,1987.

[40] D. K. Biegelsen, F. A. Ponce and J. C. Tramontana. *Simple Ion Milling Preparation of* $< 111 >$ *Tungsten Tips.* **Applied Physics Letters,** 54:1223,1989.

[41] P. K. Hansma. *Scanning Tunneling Microscopy.* **Journal of Applied Physics,** 61:R1,1989.

[42] H. -W. Fink. *Monoatomic Tips for Scanning Tunneling Microscopy.* **IBM Journal of Research and Development,** 30:460,1986.

[43] K. Ogata. *Modern Control Engineering.* Prentice-Hall, Englewood Cliffs, NJ. 1970.

[44] D. P. DiLella, J. H. Wandass, R. J. Colton and C. R. K. Marrian. *Control Systems for Scanning Tunneling Microscopes with Tube Scanners.* **Review of Scientific Instruments**,60:997,1989.

[45] G. Binnig, C. F. Quate and Ch. Gerber *Atomic Force Microscope* **Physical Review Letters**, 56:930,1986.

[46] R. Erladsson, G. M. McClelland, C. M. Mate and S. Chiang. *Atomic Force Microscopy Using Optical Interferometry.* **Journal of Vacuum Science and Technology A**, 6:266,1988.

[47] T. R. Albrecht and C. F. Quate. *Atomic Resolution Imaging of A Nonconductor by Atomic Force Microscopy.* **Journal of Applied Physics**, 62:2599,1987.

[48] B. Drake, C. B. Prater, A. L. Weisenhorn, S. A. C. Gould, T.R. Albrecht, C. F. Quate, D. S. Cannel, H. G. Hansma and P. K. Hansma. *Imaging Crystals, Polymers, and Process in Water with the Atomic Force Microscope.* **Science**, 243:1586,1989.

[49] D. Rugar, H. J. Mamin, R. Erlandsson, J. E. Stern and B. D. Terris. *Force Microscope using Fiber Optic Displacement Sensor.* **Review of Scientific Instruments**, 59:2337,1988.

[50] Y. Martin and H. K. Wickramasinghe. *Magnetic imaging by "Force Microscopy" with 1000Å Resolution.* **Applied Physics Letters**, 50:1455,1987.

[51] M. A. McCord and R. F. W. Pease. *Scanning Tunneling Microscope as a Micromechanical Tool.* **Applied Physics Letters**, 50:569,1987.

[52] M. A. McCord and R. F. W. Pease. *Lithography with the Scanning Tunneling Microscope.* **Journal of Vacuum Science and Technology B**, 4:86,1986.

[53] E. E. Ehrichs, S. Yoon and A. L. de Lozanne. *Direct Writing of 10 nm Features with the Scanning Tunneling Microscope.* **Applied Physics Letters**, 53;2287,1988.

[54] R. M. Silver, E. E. Ehrichs and A. L. de Lozanne. *Direct Writing of Submicron Metallic features with a Scanning Tunneling Microscope.* **Applied Physics Letters,** 51:247,1987.

[55] Y. Z. Li, L. Vazquez, R. Piner, R. P. Andres and R. Reifenberger. *Writing Nanometer-Scale symbols in Gold using the Scanning Tunneling Microscope.* **Applied Physics Letters,** 54:1424,1989.

[56] H. Heinzelmann, D. Anselmettl, R. Wiesendanger, H. -J. Güntherodt, E. Kaldis and A. Wisard. *Topography and Local Modification of the $HoBa_2Cu_3O_{7-x}Hi - T_c$ (001) Surface using Scanning Tunneling Microscope.* **Applied Physics Letters,** 53:2447,1988.

[57] J. S. Foster, J. E. Frommer and P. C. Arnett. *Molecular Manipulation Using a Tunneling Microscope. Nature,* 331:324,1988.

[58] T. R. Albrecht, M. M. Dovek, M. D. Kirk, C. A. Lang and C. F. Quate. *Nanometer-Scale Hole Formation on Graphite using a Scanning Tunneling Microscope.* **Applied Physics Letters,** 55;1727,1989.

[59] R. W. Keyes. *Miniaturization of Electronics and it's Limits. .* **IBM Journal of Research and Development,** 32:24,1988.

[60] E. A. Ash and G. Nichols. *Super-Resolution Aparture Scanning Microscope.* **Nature,** 237:510,1972.

[61] D. W. Pohl, W. Denk and M. Lanz. *Optical Stethoscopy: Image Recording with Resolution $\lambda/20$.* **Applied Physics Letters,** 44:651,1984.

[62] U. Ch. Fischer, U. T. Durig and D. W. Pohl. *Near-Field Optical Scanning Microscopy in Reflection.* **Applied Physics Letters,** 52:249,1988.

[63] E. Betzig, M. Isaacson and A. Lewis. *Collection Mode Near-Field Scanning Optical Microscopy.* **Applied Physics Letters,** 51:2088,1987.

[64] U. Ch. Fischer and D. W. Pohl. *Observation of Single-Particle Plasmons by Near-Field Optical Microscopy.* **Physical Review Letters,** 62:458,1989.

[65] D. Courjon, K. Sarayeddine and M. Spajer. *Scanning Tunneling Optical Microscopy.* **Optics Communications,** 71:23,1989.

[66] D. Courjon, in *Basic Concepts and Applications of Scanning Tunneling Microscopy and Related techniques,* eds R. J. Behm, N. García and H. Rohrer (Elseiver, Amsterdam, 1990).

[67] W. J. Kaiser and L. D. Bell. *Direct Investigation of Subsurface Interface Electronic Structure by Ballistic Electron Emission Microscopy.* **Physical Review Letters,** 60:1406,1988.

[68] P. Muralt and D. W. Pohl. *Scanning Tunneling Potentiometry.* **Applied Physics Letters,** 48:514,1986.

[69] P. Muralt, H. Meier, D. W. Pohl and H. W. M. Salemink. *Scanning Tunneling Microscopy and Potentiometry on a Semiconductor Heterojunction.* **Applied Physics Letters,** 50:1352,1987.

[70] J. R. Kirthley, S. Washburn and M. J. Brady. *Direct Measurement of Potential Steps at the Grain Boundaries in the Presence of Current Flow.* **Physical Review Letters,** 60:1546,1988.

[71] J. P. Pelz and R. H. Koch. *Extremely Low-Noise Potentiometry with Scanning Tunneling Microscope* . **Review of Scientific Instruments,** 60:301,1989.

[72] H. W. Fink. *Point Source for Ions and Electrons.* **Physica Scripta,** 38:260,1988.

[73] H. W. Fink, in *Basic Concepts and Applications of Scanning Tunneling Microscopy and Related techniques,* eds R. J. Behm, N. García and H. Rohrer (Elseiver, Amsterdam, 1990).

[74] R. Allenspach and A. Bischof. *Spin-Polarized Secondary Electrons from a Scanning Tunneling Microscope in Field Emission Mode.* **Applied Physics Letters,** 54:587,1989.

[75] J. K. Gimzewski, B. Reihl, J. H. Coombs and R. R. Schlitter. *Photon Emission with the Scanning Tunneling Microscope.* **Zeitschrift für Physik B.** 72:497,1988.

[76] A. P. Fein, J. R. Kirthley and M. W. Shafer. *Tunneling Measurements of the Dependence of the Energy Gap on Critical Temparature in* $La_{2-x}Sr_xCuO_4$. **Physical Review B.** 37:9738,1988.

[77] R. M. Feenstra, in *Basic Concepts and Applications of Scanning Tunneling Microscopy and Related techniques,* eds R. J. Behm, N. García and H. Rohrer (Elseiver, Amsterdam, 1990).

[78] J. Weber. **Physical Review,** 117:306,1960, P.F. Michelson, J. C. Price and R. C. Taber. **Science,** 237:150,1987.

[79] M. Niksch and G. Binnig. *Proposal for a Novel Gravitational-Wave Sensor.* **Journal of Vacuum Science and Technology A,** 6:470,1988.

[80] D. G. Blair, A. Giles and M. Zeng. *Impedance Matching Element for a Gravitational Wave Detector.* **Journal of Physics D,** 20:162,1987.

[81] M. F. Bocko, K. A. Stephenson and R. H. Koch. *Vacuum Tunneling Probe: A Non-Reciprocal, Reduced Back-Action Transducer.* **Physical Review Letters,** 61:726,1988.

[82] D. P. E. Smith, in *Basic Concepts and Applications of Scanning Tunneling Microscopy and Related techniques,* eds R. J. Behm, N. García and H. Rohrer (Elseiver, Amsterdam, 1990).

[83] J. R. Matey and J. Blanc. *Scanning Capacitance Microscopy.* **Journal of Applied Physics,** 47:1437,1985.

[84] C. C. Williams, W. P. Hough and S. A. Rishton. *Scanning Capacitance Microscopy on a 25nm Scale.* **Applied Physics Letters,** 55:203,1989.

[85] P. K. Hansma, B. Drake, O. Marti, S. A. C. Gould and C. B. Prater. *The Scanning Ion-Conductance Microscope.* **Science,** 243:641,1989.

[86] M. Amrein, A. Stasiak, H. Gross, E. Stoll and G. Travaglini. *Scanning Tunneling Microscopy of recA-DNA Complexes Coated with a Conducting Film.* **Science,** 240:514,1988.

[87] A. Cricenti, S. Selci, A. C. Felici, R. Generosi, E. Gori, W. Djaczenko and G. Chiarotti, in *Basic Concepts and Applications of Scanning Tunneling Microscopy and Related techniques,* eds R. J. Behm, N. García and H. Rohrer (Elseiver, Amsterdam, 1990).

[88] M. M. Dovek, T. R. Albrecht, S. W. J. Kuan, C. A. Lang, R. Emch, P. Grutter, C. W. Frank, R. F. W. Pease and C. F. Quate. *Observation and Manipulation of Polymers by Scanning Tunneling and Atomic Force Microscopy.* **Journal of Microscopy,** 152:229,1988.

[89] D. P. E. Smith, A. Bryant, C. F. Quate, J. P. Rabe, Ch. Gerber and J. D. Swalen. *Images of a Lipid Bilayer at Molecular Resolution by Scanning Tunneling Microscopy.* **Proc. Acad. Sci. USA,** 84:969,1987.

[90] J. S. Foster and J. E. Frommer. *Imaging of Liquid Crystals using a Tunneling Microscope.* **Nature,** 333:542,1988.

[91] D. P. E. Smith, H. Hörber, Ch. Gerber and G. Binnig. *Smectic Liquid Crystal Monolayers on Graphite Observed by Scanning Tunneling Microscopy.* **Science,** 245:43,1989.

[92] H. Ohtani, R. J. Wilson, S. Chiang, C. M. Mate. *Scanning Tunneling Microscopy Observations of Benzene Molecules on the Rh(111)-(3 × 3) ($C_6H_6 + 2CO$) Surface.* **Physical Review Letters,** 60:2398,1988.

[93] D. J. Trevor, C. E. D. Chidsey and D. N. Loiacono. In Situ *Scanning Tunneling Microscope Observation of Roughening and Annealing, and Dissolution of Gold(111) in an Electrochemical Cell.* **Physical Review Letters,** 62:929,1989.

[94] C. W. Lin, Fu-Ren F. Fan and A. J. Bard. *High Resolution Photoelectrochemical Etching of n-GaAs with the Scanning Electrochemical and Tunneling Microscope.* **J. Electrochemical Soc. 134:1038,1987.**

[95] I. P. Batra, N. Garcia, H. Rohrer, H. Salemink, E. Stoll and S. Ciraci. *A Study of Graphite Surface with STM and Electronic Structure Calculations.* **Surface Science,** 181:126,1987.

[96] R. C. Tatar and S. Rabii. *Electronic Properties of Graphite: A Unified Approach.* **Physical Review, B** 25:4126,1982.

[97] A. Selloni, P. Carnevalli, E. Tosatti and C. D. Chen. *Voltage-dependent Scanning Tunneling Microscopy of a Crystal Surface: Graphite.* **Physical Review, B** 31:2602,1985.

[98] H. A. Mizes, Sang-Il Park and W. A. Harrison. *A Multiple Tip Interpretation of Anomalous Scanning Tunneling Microscopy Images of Layered Materials.* **Physical Review, B** 36:4497,1987.

[99] Sang Il Park, J. Nogami, H. A. Mizes and C. F. Quate. *Chemical Dependence of the Multiple-tip Effect in Scanning Tunneling Microscopy.* **Physical Review, B** 38:4269,1988.